Intercomparison of wind and wave data from the ECMWF Reanalysis Interim and the NCEP Climate Forecast System Reanalysis

CrossMark

Justin E. Stopa [1], Kwok Fai Cheung *

Department of Ocean and Resources Engineering, University of Hawaii at Manoa, Honolulu, HI 96822, USA

A B S T R A C T

The recent release of the ECMWF Reanalysis Interim (ERA-I) and NCEP Climate Forecast System Reanalysis (CFSR) allows for studies of global climate and its cycles with unprecedented detail. While the developers have performed verification and validation, there is little information on their relative performance in particular related to their use in ocean modeling. This study focuses on the intercomparison of wind speeds and wave heights from ERA-I and CFSR utilizing the same set of altimetry and buoy observations and error metrics to assess their consistency in time and space. Both products have good spatial homogeneity with consistent levels of errors in the Northern and Southern Hemispheres. ERA-I proves to be homogenous through time, while CFSR exhibits an abrupt decrease in the level of errors in the Southern Ocean beginning 1994. ERA-I generally underestimates the wind speed and wave height with lower standard deviations in comparison to observations, but maintains slightly better error metrics. Despite having a small positive bias, CFSR provides a better description of the variability of the observations and improved performance in the upper percentiles associated with extreme events. Overall ERA-I has better homogeneity through time deeming it more reliable for modeling of long-term processes; however caution must be applied with analysis of the upper percentiles.

© 2013 Elsevier Ltd. All rights reserved.

1. Introduction

Studies of wind and wave climate require datasets of sufficient duration and adequate resolution. Datasets with long time series have additional applications essential for maritime commerce, infrastructure design, and hazard mitigation. Voluntary observing ships, satellite altimetry, synthetic aperture radar (SAR), and buoys have been the source of measurements. Ship data has the longest duration but varied quality, sparse coverage, and limited extreme events due to shipping routes (Gulev et al., 2003). Satellite altimetry covers a large expanse of the ocean with high precision measurements. Despite being limited to only a few sea state parameters, it has provided a valuable resource for climate studies (e.g., Young, 1999; Woolf et al., 2002; Chen et al., 2002; Hemer et al., 2010; Young et al., 2011). SARs have the ability to provide a frequency-direction spectrum of the sea state for parameterization of wave processes (Hasselmann and Hasselmann, 1991; Hwang et al., 2013). Buoys provide the most comprehensive measurements and present a critical source of information (e.g., Bromirski et al., 2005; Menendez et al., 2008; Genmrich et al., 2011).

The data, however, is limited to discrete locations with the majority in the Northern Hemisphere.

Recent advances in numerical modeling have greatly supplemented the various sources of wind and wave measurements with higher spatial and temporal resolution. Forecast models have been operational for at least two decades in the National Centers for Environmental Predictions (NCEP) and the European Centre for Medium-Range Weather Forecasts (ECMWF). The archived operational forecasts have provided an important source of wind and wave information to the community. The datasets, however, exhibit inhomogeneity due to upgrades in model physics, resolution, and assimilation techniques over the years, deeming unsuitable for the analysis of multi-year climate signals. Reanalysis incorporates observations from a wide range of platforms, while implementing the same model and data assimilation technique for consistency. The constantly improving quality, coverage, and resolution of the observations used in the assimilation may still represent a source of non-physical variations that require attention in modeling of ocean wave climate (Hines et al., 2000; Kistler et al., 2001; Sterl, 2004; Reguero et al., 2012; Chawla et al., 2013; Rascle and Ardhuin, 2013).

Well-established datasets include the NCEP global Reanalysis I (R1) and Reanalysis II (R2) at 1.9° resolution and the ECMWF ERA-15 and ERA-40 at 1.5° resolution (Kalnay et al., 1996; Kanamitsu

* Corresponding author. Tel.: +1 (808) 956 3485; fax: +1 (808) 956 3498.
   E-mail addresses: stopa@hawaii.edu (J.E. Stopa), cheung@hawaii.edu (K.F. Cheung).
   [1] Tel.: +1 (808) 956 8198; fax: +1 (808) 956 3498.

et al., 2002; Sterl et al., 1998; Uppala et al., 2005). While the ECMWF datasets are derived from a coupled atmosphere-wave model, the NCEP R1 wind data is typically used to force a wave model separately. For example, Cox and Swail (2001) implemented a second-generation wave model with R1 winds to produce 40 years of global wave hindcast. Caires et al. (2004) performed an inter-comparative study of these reanalysis datasets and identified their strengths and weaknesses. Newly available datasets, such as the NCEP Climate Forecast System Reanalysis (CFSR) and the ECMWF Reanalysis Interim (ERA-I), have updated physics, improved assimilated data, and higher resolution of 0.3° and 0.7° respectively (Saha et al., 2010; Dee et al., 2011). Similar to ERA-40, ERA-I is a coupled atmosphere-wave model producing a wind and wave dataset. Chawla et al. (2013) utilized the CFSR surface winds at 0.5° to hindcast the global wave conditions the third generation spectral model WAVE-WATCH III (WW3) of Tolman et al. (2002). This is NCEP's first official release of a reanalysis wave dataset, which we refer to as CFSR Waves (CFSR-W) throughout this article.

CFSR and ERA-I, which have improved performance compared to their respective predecessors R1 and ERA-40, represent an important data source of atmospheric forcing for the ocean modeling community. It is essential to know how the two latest reanalysis datasets perform in relation to each other since they have different resolutions, constituent models, physics, and assimilation techniques. An objective assessment of the product homogeneity in time and space will increase confidence in the datasets for application in climate research. This study utilizes buoy and altimetry observations to compare the performance, validity, and consistency of the CFSR and ERA-I datasets. Section 2 summarizes the background information of the two reanalysis datasets and provides details of the observations from buoys and altimeters. Section 3 describes the methodology and error metrics used in the inter-comparison. The results are presented in Section 4 with subsections dedicated to the wind and waves separately. We first identify the patterns and trends and then allude to their interrelations and explanations. A summary of the major findings is given in Section 5 to conclude the study.

2. Reanalysis and observation datasets

2.1. Reanalysis datasets

Saha et al. (2010) have demonstrated improved performance of CFSR in comparison to its predecessors, R1 and R2, also developed at NCEP. The main advancements include coupling between the ocean, atmosphere, and land surface, an interactive sea ice model, assimilation of satellite radiances, and increased horizontal and vertical resolution in the atmospheric model. The Global Forecast System (GFS) of Yang et al. (2006) constitutes the atmospheric model, which has ~38 km horizontal resolution and 64 vertical layers extending from the surface to 0.26 hPa. The Geophysical Fluid Dynamic Lab's Modular Ocean Model (MOM) version 4 describes the ocean circulation at 0.25° resolution in the equatorial
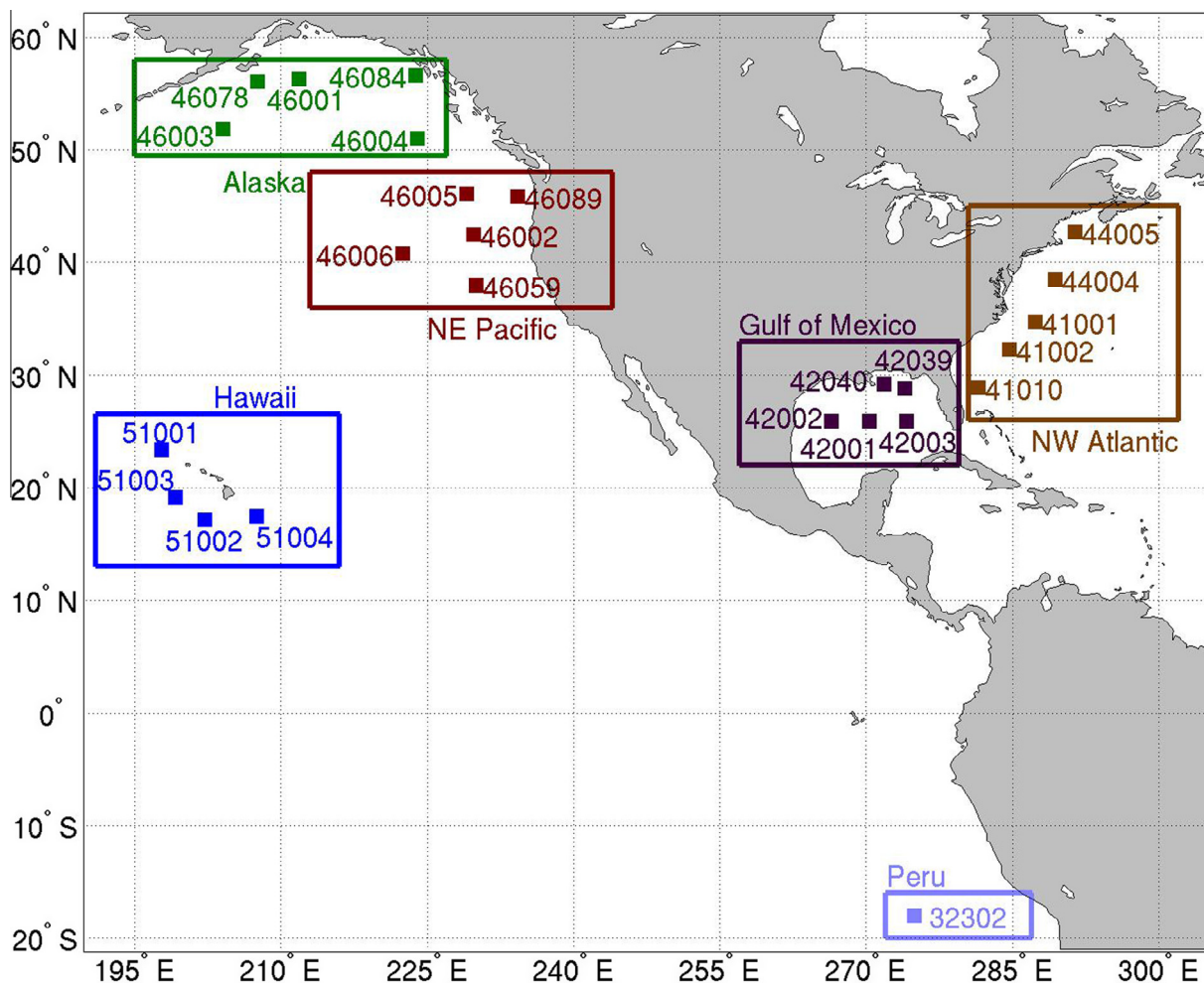

Fig. 1. Buoy locations grouped by regions.

region and 0.5° above the tropics with 40 levels extending to 4737 m depth. The NOAH land model of Ek et al. (2003) includes 4 soil layers and the ice model of Wu et al. (2005) has 2 layers to account for variations below the surface. Prior reanalysis efforts with R1, R2, ERA-15, and ERA-40, have laid the groundwork and best practice to assemble and convert observations into an internationally agreed upon data format for model assimilation (Kleist et al., 2009). CFSR uses the same model and data assimilation techniques in three space dimensions (3D-Var) at the each initialization of the model hindcast.

CFSR does not have a model component for ocean surface waves. Chawla et al. (2013) utilized WAVEWATCH III (WW3) of Tolman et al. (2002) and wind forcing at 0.5° from CFSR to reproduce the wave conditions for 1979–2009. WW3 is a phased-averaged model that evolves the action density for a range of frequencies and 360° of directions under wind forcing and geographical constraints. Features smaller than the grid spacing, such as smaller islands and atolls are accounted for by prorating the energy transfer through a given computational cell (Tolman, 2003; Chawla and Tolman, 2008). The physical processes are governed by the action balance equation with the source terms accounting for nonlinear effects such as wind–wave interactions, quadruplet wave–wave interactions, and dissipation through whitecapping, bottom friction, and wave breaking. The source term package from Tolman and Chalikov (1996) was implemented as the first stage of the NOAA Partnership Program (NOPP) initiative to improve wave modeling (Tolman et al., 2013). Hourly surface winds at 10-m elevation along with the temperature difference between the ocean and atmosphere from CFSR provided the forcing to WW3. Passive microwave sensors aboard the SMM/R and SSM/I satellites were used to define the reanalysis daily ice concentrations at 0.5° resolution. The hindcast consists of a mosaic of 16 computational grids with resolution ranging from 1/2° to 1/15°. For the present study, only data from the global grid at 0.5° and 3 h increment are utilized.

ERA-I (release Cy31r2) is the most up-to-date reanalysis product of ECMWF available for 1979-present. Dee et al. (2011) showed its improved performance in comparison to ERA-40 due to the use of additional observations, updated data assimilation techniques, increased resolution, and better physics in the models. ECMWF's Integrated Forecast System (IFS) incorporates three fully coupled models of the atmosphere, land surface, and ocean waves. The atmospheric model has approximately ∼79 km grid spacing and 37 pressure levels extending from the surface to 0.1 hPa. The land surface model uses the tiled ECMWF scheme to evolve the thermal and water content exchanges in four layers (Viterbo and Betts, 1999). ERA-I assimilates data in four dimensions (4D-Var), which Whitaker et al. (2009) have shown to outperform 3D-Var assimilation techniques. ERA-I utilizes the WAve Model known as WAM (WAMDIG, 1988), which is a third-generation spectral model based on the same governing equation as WW3. The updated WAM source terms from Bidlot et al. (2005, 2007) and Janssen (2008) better describe the physical phenomenon of wave growth and dissipation. The two-way coupling scheme in ERA-I passes the wind fields and other atmospheric parameters that influence wave growth to WAM and information is returned regarding the surface roughness by use of the Charnock parameter (Janssen, 1991).

ERA-I also includes assimilation of measured significant wave heights from polar orbiting satellites to constrain the predicted wave spectra. The reprocessed wave measurements from European Remote Sensing Satellites 1 and 2 (ER1 and ER2), Environmental Satellite (ENV), JASON-1 (JS1), and JASON-2 (JS2) have been incorporated into their data assimilation since 1991, but the sparse data may become a source of spatial inhomogeneity in the wave field. Bidlot et al. (2005) reported a slight change of the bias in the model data most notably in the South Pacific due to assimilation of observed wave heights beginning in 1991. The assimilated wave model is resolved on a ∼0.7° grid using 24 directions and 30 frequencies and data is available every 6 h and the results are directly implemented in the present study.

2.2. Observation datasets

Both buoys and satellite altimeters provide measurements to compare with the reanalysis datasets. The National Oceanographic Data Center (NODC) provides quality controlled records of wind speeds and significant wave heights from buoys (http://www.nodc.noaa.gov/BUOY/). Fig. 1 shows the locations of 25 National Data Buoy Center (NDBC) buoys selected for this study. The buoys are chosen because they are deep water and far from coastlines and typically have time series covering a large portion of the 31 years analyzed. Direct comparison can be made to prior studies of reanalysis data that typically used a subset of these buoys (Caires et al., 2004; Chawla et al., 2013; Reguero et al., 2012). The wind speed measurements have been included in the Comprehensive Ocean–Atmosphere Data Set (COADS) as noted by Woodruff et al. (1998) and possibly some were assimilated into CFSR. However, the significant wave height records from these buoys were not used in the production of either ERA-I or CFSR-W datasets, thus representing an independent source of information for validation.

Altimetry covers a large expanse of the oceans allowing better spatial validation of the wind and wave data. Zieger et al. (2009)
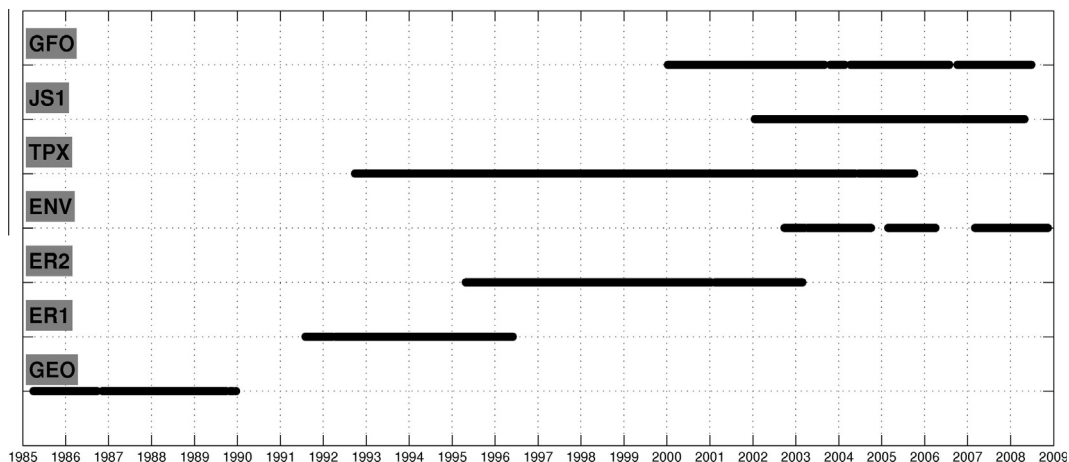

Fig. 2. Available altimetry observations from 1985 to 2010.

Table 1
Error metrics for wind speed at buoys using all available data during 1979–2009.

Wind Speed									
Region	n	Average (m/s)	Reanalysis	NBIAS (%)	RMSE (m/s)	CRMSE	COR	SI (%)	NSTD
Peru	70,360	6.57	CFSR	6.14	1.37	1.31	0.81	19.87	0.88
			ERA-I	0.54	1.02	1.02	0.88	15.52	0.80
Hawaii	71,6480	7.50	CFSR	−3.90	1.37	1.34	0.86	17.82	0.88
			ERA-I	−5.70	1.26	1.18	0.89	15.69	0.76
Gulf of Mexico	883122	6.11	CFSR	0.42	1.52	1.52	0.87	24.81	0.85
			ERA-I	−4.98	1.41	1.36	0.90	22.32	0.75
NW Atlantic	105,8995	7.08	CFSR	4.23	1.73	1.70	0.89	24.01	0.98
			ERA-I	−1.70	1.56	1.55	0.90	21.91	0.83
Alaska	542,834	8.15	CFSR	3.90	1.70	1.66	0.91	20.42	1.05
			ERA-I	0.91	1.56	1.56	0.92	19.14	0.91
NE Pacific	713,020	7.63	CFSR	2.38	1.50	1.49	0.91	19.48	1.02
			ERA-I	0.69	1.33	1.33	0.93	17.44	0.92

provided quality controlled altimetry data against buoy measurements for comparison with the reanalysis datasets. They considered seven altimeter missions with global coverage of the significant wave height and wind speed derived from the Ku-microwave band. Fig. 2 lists the platforms and their periods of operation spanning 23 years since 1985. The calibrated data from these platforms shows a consistent level of accuracy with the root-mean-square (RMS) errors less than 0.25 m for the significant wave height and 1.7 m/s for the 10-m wind speed. It should be pointed out the post-processing of the altimetry winds using the 1-paramater Ku-microwave band has been shown to be inaccurate in low wind speeds (Gourrion et al., 2002). Data sets collected by GEOSAT Follow-On (GFO), its predecessor GEOdetic SATellite

(GEO), and TOPEX/Posedion (TPX) were not used in the reanalysis assimilation providing an independent source for validation. However, a systematic instrumental bias exists in the GEO wind data that excludes its use in the comparison here.

3. Methodology

The buoy and altimetry measurements represent a large volume of spatial and temporary data that requires a systematic approach for their intercomparison with the ERA-I and CFSR-W datasets. The objective is to assess the validity and consistency of each reanalysis dataset by independent measurements not
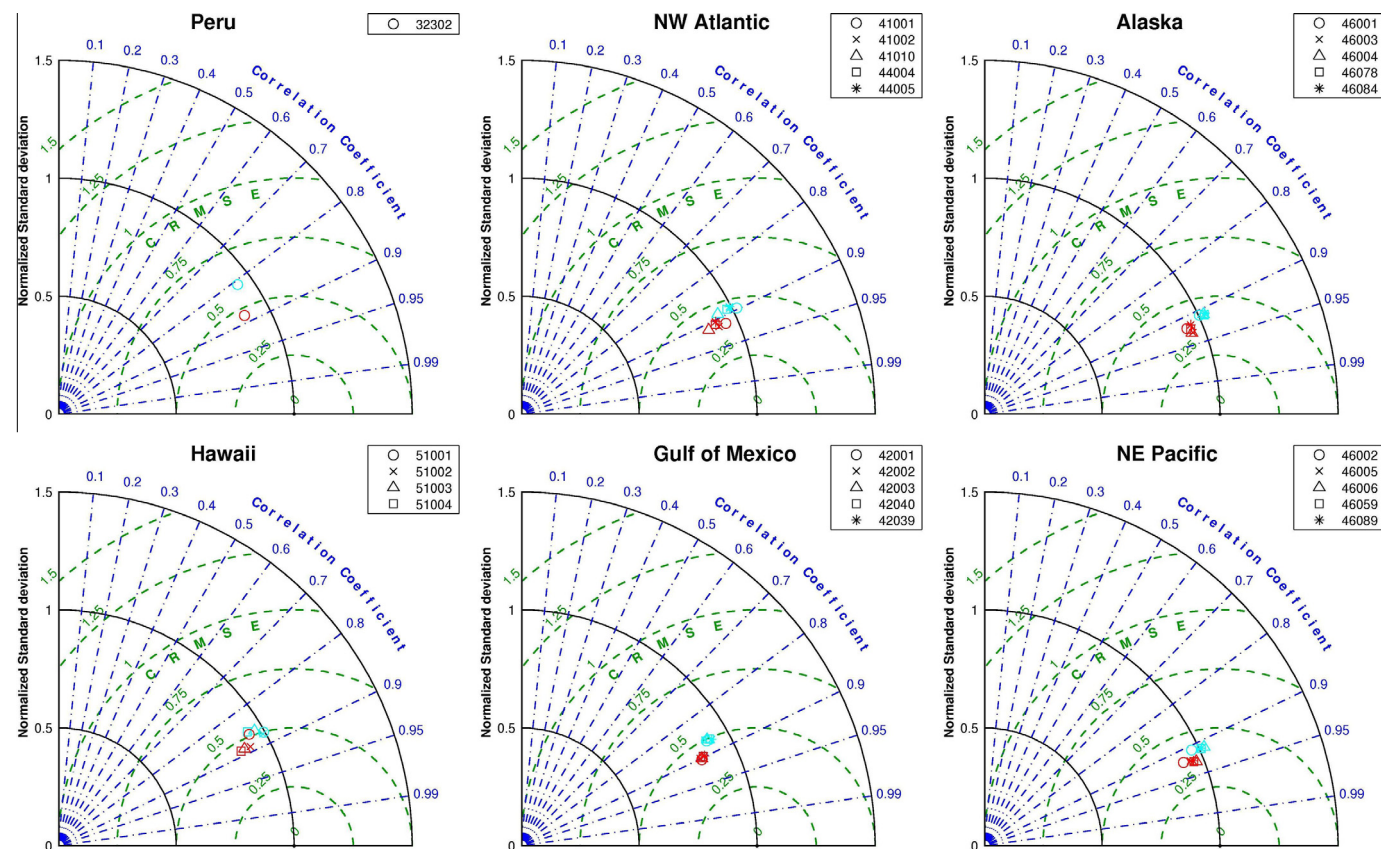

Fig. 3. Taylor diagram of error metrics for wind speed at buoys grouped by region. Cyan symbols represent CFSR and red symbols represent ERA-I. A perfect model would lie on the x-axis with a NSTD equal to one.
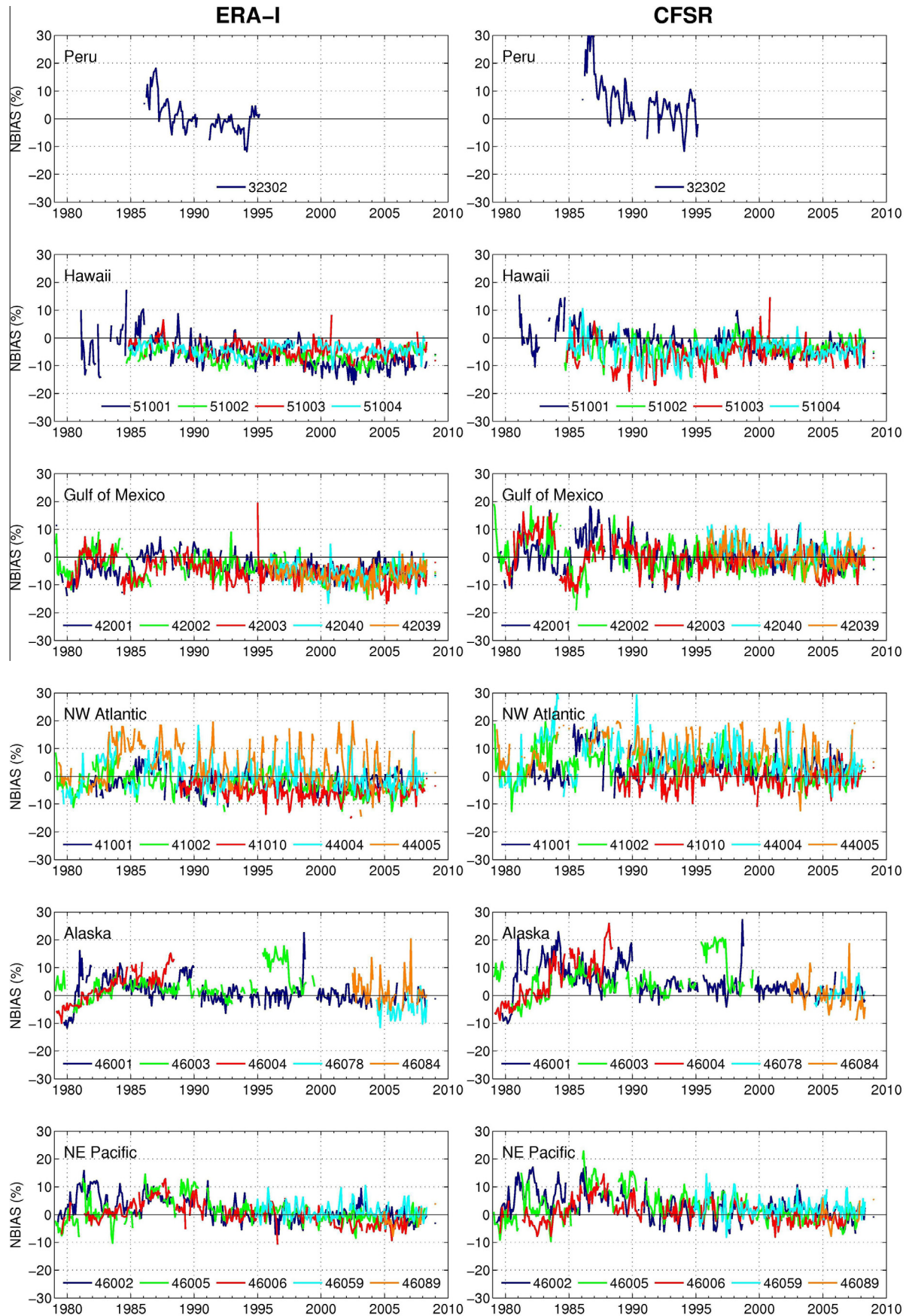
Fig. 4. Normalized wind speed biases for buoys by region.

used in the assimilation whenever possible. The 25 buoys are grouped into the six regions as shown in Fig. 1 each with similar environmental conditions. The wind speed observations are all adjusted to the 10-m standard elevation using a logarithmic profile under the assumption of neutral stability, which is used in the absence of the vertical temperature flux measurements. The quality controlled altimetry measurements by Zieger et al. (2009) have spacing of approximately 5.8 km and are available every second along the satellite track. Their wind speeds were estimated from the surface stress also assuming a neutrally stable atmosphere. The altimetry measurements are smoothed by a running mean of 15 adjacent points that covers a distance comparable to the grid spacing (Chawla et al., 2013). Gridded wind speeds and significant wave heights from CFSR-W and ERA-I are linearly interpolated in time and space to match the buoy and altimetry observations. The altimetry measurements allow assessment of spatial patterns across the globe. To examine the variation over time, we provide spatially integrated results for the Northern Hemisphere (north of 20°N), Equatorial region (20°S–20°N), and the Southern Hemisphere (south of 20°S).

We use a number of error metrics to measure the difference between the observed and reanalysis data. Let x and y denote the observed and computed values of the wind speed or significant wave height over time. The normalized bias, root-mean-square error, correlation coefficient, scatter index, and normalized standard deviation are defined as

$$NBIAS = \frac{\bar{x} - \bar{y}}{\sqrt{\frac{1}{n}\sum_{i=1}^{n}(x_i)^2}}, \tag{1}$$

$$RMSE = \sqrt{\frac{1}{n}\sum_{i=1}^{n}(y_i - x_i)^2}, \tag{2}$$

$$COR = \frac{\sum_{i=1}^{n}(y_i - \bar{y})(x_i - \bar{x})}{\sqrt{\sum_{i=1}^{n}(y_i - \bar{y})^2}\sqrt{\sum_{i=1}^{N}(x_i - \bar{x})^2}}, \tag{3}$$

$$SI = \frac{1}{\bar{x}}\sqrt{\frac{1}{n}\sum_{i=1}^{n}[(y_i - \bar{y}) - (x_i - \bar{x})]^2}, \tag{4}$$

$$NSTD = \frac{\sqrt{\frac{1}{n}\sum_{i=1}^{n}(y_i - \bar{y})^2}}{\sqrt{\frac{1}{n}\sum_{i=1}^{n}(x_i - \bar{x})^2}}, \tag{5}$$

where the over bar indicate mean values through time and n denotes the number of data pairs. Taylor (2001) proposed a graphical approach to describe how well one dataset matches the other in terms of the *NSTD*, *COR*, and the normalized centered *RMSE*, which is defined as
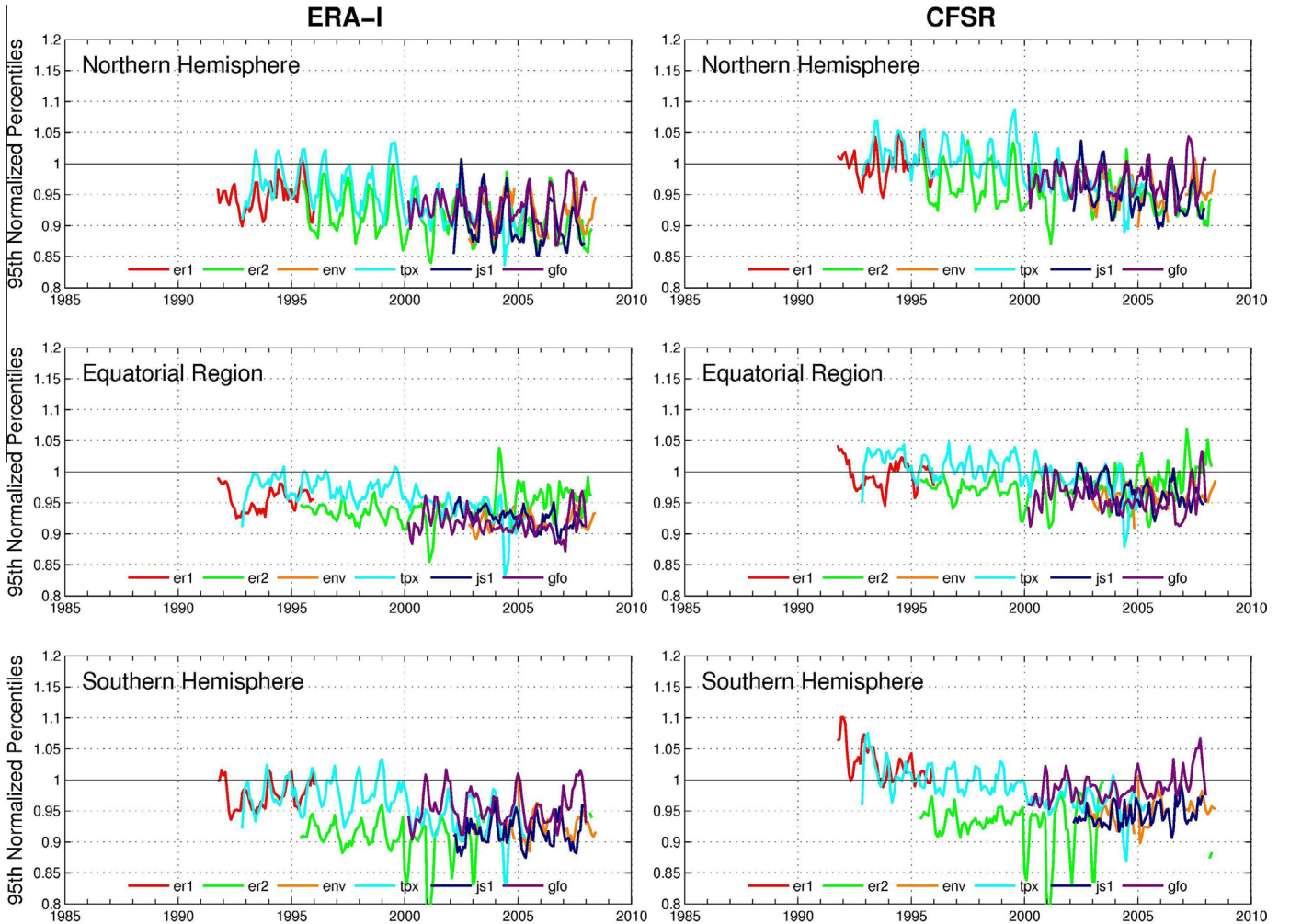

Fig. 5. The 95th percentile wind speed normalized by altimetry observations and integrated across the Northern Hemisphere, Equatorial region, and Southern Hemisphere.

$$CRMSE = \frac{\sqrt{\left(\frac{1}{n}\sum_{i=1}^{n}(y_i - \bar{y}) - (x_i - \bar{x})\right)^2}}{\sqrt{\left(\frac{1}{n}\sum_{i=1}^{n}(x_i - \bar{x})\right)^2}}. \tag{6}$$

The *NBIAS*, *CRMSE*, and *NSTD* are normalized by the observations to allow comparison across different locations and time periods. It should be pointed out that the observations also contains errors and are simply used as a reference for the inter-comparison.

The Mann–Kendall (MK) technique with Sen's slope is a non-parametric test that detects data consistency and trend through time (Mann, 1945; Kendall, 1975; Sen, 1968). Hirsch et al. (1982) generalized the MK test to account for seasonal cycles, which would otherwise lead to a biased estimate. We use the technique to evaluate the trend of the monthly error ε between x and y at a given percentile. The MK statistic and its variance are computed for each month across all years. The procedure begins with computation of the Sen's slope for the kth month

$$Q_k = \frac{\varepsilon_{kj} - \varepsilon_{ki}}{j - i}, \tag{7}$$

where i and j are indices in the time series such that $j > i$. The median of Q_k gives an unbiased estimate of the slope. The corresponding MK statistic S_k and its variance are defined as

$$S_k = \sum_{i=1}^{n_k-1} \sum_{j=i+1}^{n_k} \mathrm{sgn}(\varepsilon_{kj} - \varepsilon_{ki}), \tag{8}$$

$$VAR(S) = \frac{1}{18}[n(n-1)(2n+5)]. \tag{9}$$

The overall statistic and variance are computed for all 12 months as

$$S' = \sum_{k=1}^{12} S_k, \tag{10}$$

$$VAR(S') = \sum_{k=1}^{12} VAR(S_k) + \sum_{k=1}^{12}\sum_{l=1}^{12} \mathrm{cov}(S_k S_l), \tag{11}$$

where $k \neq l$ and *cov* represents the covariance. The null hypothesis is tested using the *Z*-statistic

$$Z' = \begin{cases} \frac{S'-1}{\sqrt{VAR(S')}} & \text{if } S' > 0 \\ 0 & \text{if } S' = 0 \\ \frac{S'+1}{\sqrt{VAR(S')}} & \text{if } S' < 0 \end{cases} \tag{12}$$

against the normal distribution (Gilbert, 1987). A trend exists if $|Z| > Z_{1-\alpha/2}$, where α defines a statistically significant level. The technique has been applied extensively in hydrology and also to ocean waves by Wang and Swail (2001) and Young et al. (2011).
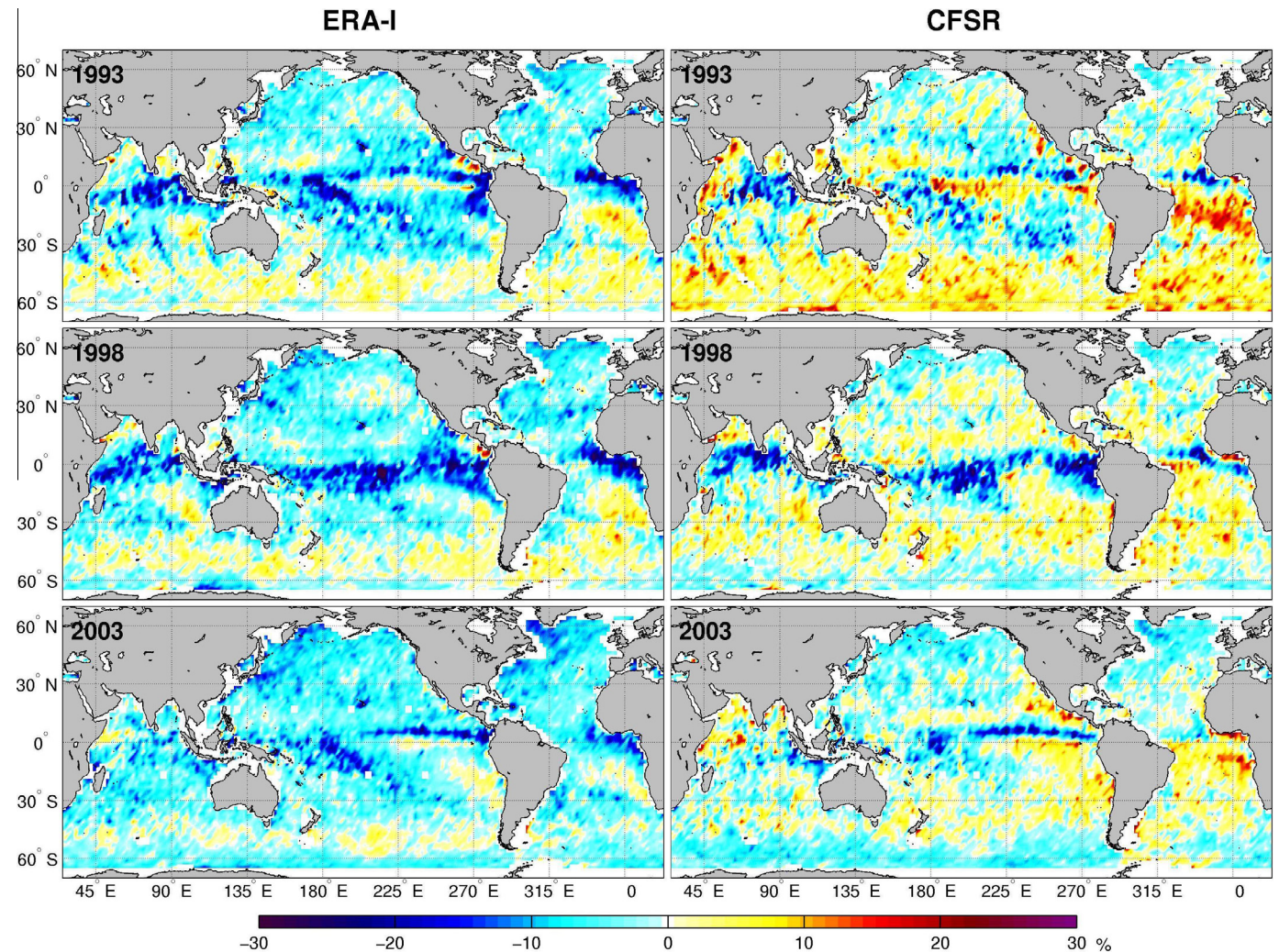

Fig. 6. Normalized wind speed biases for TPX in December–January–February (DJF).

4. Inter-comparison of ERA-I and CFSR-W

ERA-I and CFSR-W represent major advancements in global reanalysis since the comprehensive assessment performed by Caires et al. (2004). To set a baseline for the inter-comparison, we utilized their methodology to provide a consistent analysis of the two datasets in relation to the predecessors listed in Table S1 of the supplementary material. Tables S2–S6 and S7–S11 summarize the error metrics for the wind speed and significant wave height. The results show the CFSR and ERA-I wind data performs superior to those of R1 and ERA-40 with lower RMSEs, lower scatter indices, and better correlation. The corresponding comparisons of the wave data for CFSR-W and ERA-I also show a similar level of improvement. The errors in the Northern and Southern Hemispheres are comparable for the new datasets showing improved spatial consistency of the products. Both ERA-I and CFSR-W winds have the largest errors in the Equatorial region that might result from the lack of atmospheric stability considerations in deducing the measured data. Since this is a relatively calm and not a major wave generation region, the errors in the waves are lower in comparison to the wind data. The overall comparison shows significant improvements in ERA-I and CFSR-W and confirms they are at the best available reanalysis datasets from ECMWF and NCEP.

4.1. Wind speed

The grouping of the buoys by similar environment allows computation of representative error metrics in each region for inter-comparison of ERA-I and CFSR. Table 1 summarizes the aggregated error metrics of the winds for the six regions. The comparison involves large numbers of buoy records and the average values provide an indication of the local environment. The Taylor diagrams in Fig. 3 confirm the data consistency at the individual buoys while illustrating the variability between the two reanalysis datasets. In general, ERA-I has better comparisons than CFSR with lower RMS and CRMS errors, larger correlation coefficients, and smaller scatter indices. CFSR typically overestimates the wind speed except near Hawaii, but ERA-I has low negative biases for all regions. The normalized standard deviation reveals that ERA-I has lower variability than the observations by 10–20%. CFSR matches the variability very well but has slightly higher values than the observations near Alaska and in the NE Pacific. The large scatter indices in the Gulf of Mexico and the NW Atlantic might be a result of the larger wind variability and reduced performance of model parameterizations for short fetches (Bidlot et al. 2005, 2007; Ardhuin et al. 2007). The neutral stability assumption in converting the observed data standard 10-m elevation may also contribute to the larger scatter indices in these regions.
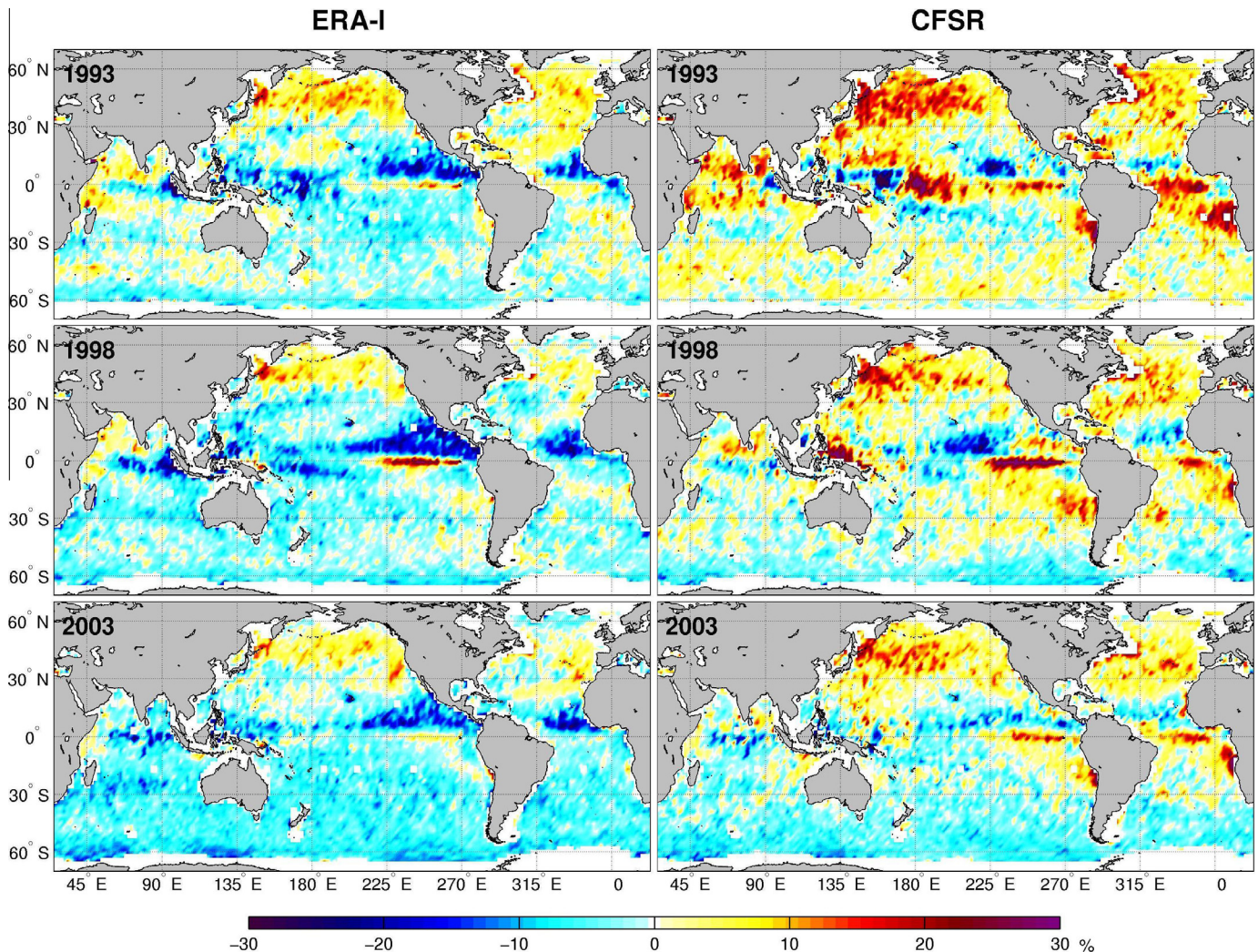

Fig. 7. Normalized wind speed biases for TPX in June–July–August (JJA).

Fig. 4 shows the normalized monthly biases between the recorded and reanalysis winds to illustrate the variability of errors over time. The most notable features are the large seasonal cycles with predominant negative biases in high seasons and vice versa. Buoy 32302 near Peru provided essential information of the Southern Hemisphere trade winds. CFSR gives higher predictions of the wind speed than ERA-I in particular for the early period around 1986–1987. The buoys near Hawaii measure the year-round trade winds in the Northern Hemisphere. ERA-I and CFSR are comparable with average negative biases around 6% throughout. In the Gulf of Mexico, ERA-I also consistently underestimates the wind speed around 6%. CFSR has a better match to the buoy observations, but with larger seasonal variability ranging ±20%. The buoys in NW Atlantic recorded a mix of extra-tropical and trade wind conditions. Both datasets have large seasonal biases, but ERA-I has average values closer to zero. Extra-tropical storms dominate in the Alaska region and influence the weather in NE Pacific. The results show reduced seasonal variations in comparison to other regions. In general, CFSR tends to give higher predictions of the wind speed and larger positive biases than ERA-I. Other than that, both datasets exhibit similar features including anomalous weather events that either dataset is not able to reproduce. These include large positive trends or modulations in the 1980s and a reduction of the bias in the early 1990s. This is most likely due to improvement in the quality and quantity of the assimilated wind data with the introduction of the SSM/I in 1994.

Satellite altimetry provides independent wind measurements not used in the assimilation to evaluate the reanalysis winds across the globe from 1992 onward. Fig. 5 shows the monthly 95th percentile of the reanalysis wind speed normalized by the corresponding altimetry measurements in the Northern Hemisphere, Equatorial region, and Southern Hemisphere. The comparison at the 95th percentile offers a more rigorous test than the normalized bias for conditions that have more influence on wave generation. As in the buoy comparison, the results show strong seasonal variations with a range of 15% in the Northern and Southern Hemispheres. The comparison reflects the decreased seasonal variability in the Equatorial region associated with the consistent weather year round. Both datasets generally underestimate the stronger winds at the 95th percentile. ERA-I underestimates the measurements by 8% on average, while CFSR matches the observations better with underestimations of around 3%. In the Southern Hemisphere, the comparison with the ER2 measurements shows anomalous features in the beginning of the years 2000–2004 in both datasets that are not evident with data from the other platforms and may be due to the sea state bias. These anomalous features are also evident in the post-processed ER2 measurements of Queffeulou and Croizé-fillon (2012). Overall, the CFSR bias shows a decreasing trend through 1994. While Chawla et al. (2013) and
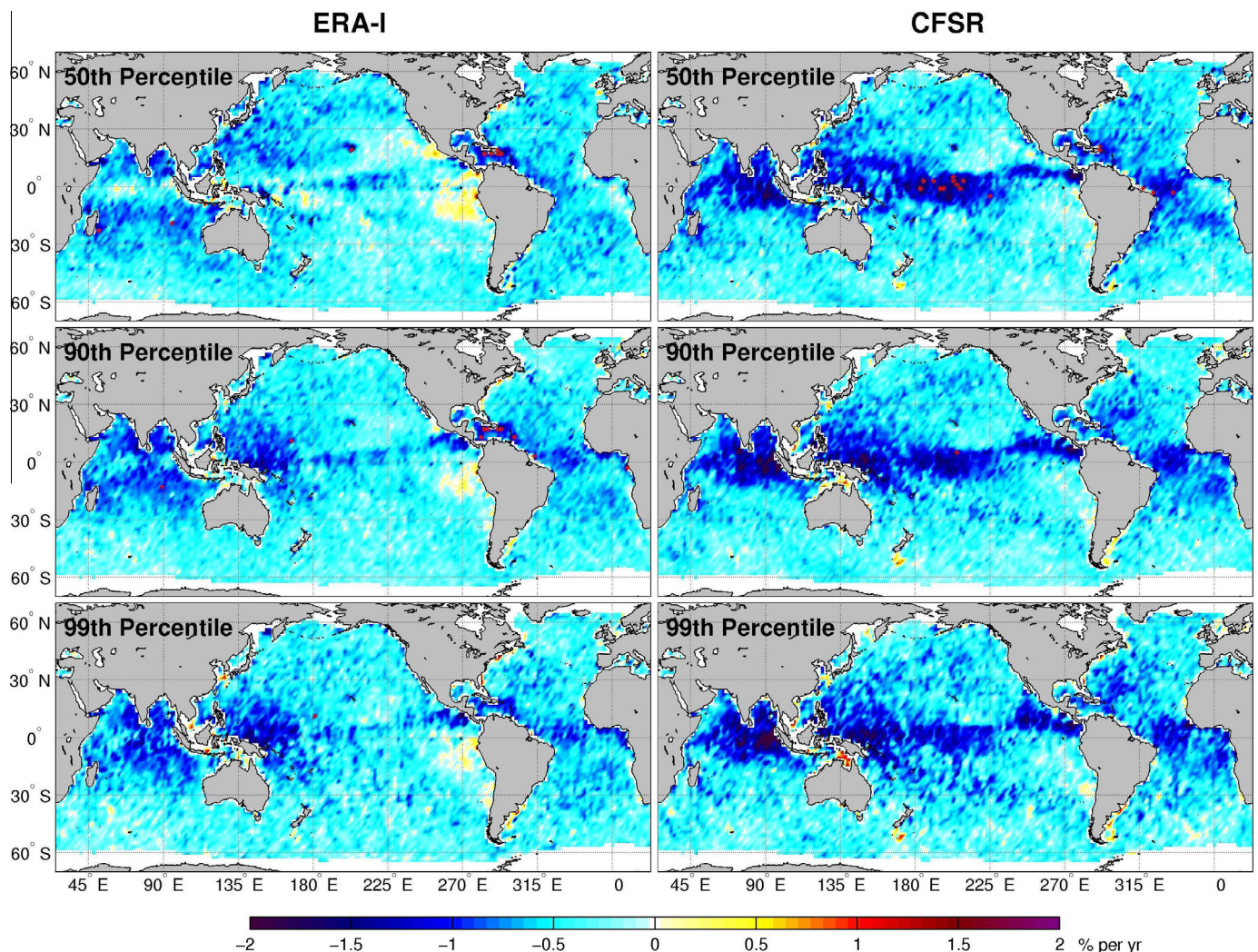

Fig. 8. Sen's slope with statistically significant results from the seasonal MK test of normalized monthly wind speed percentiles using TPX and GFO. Statistically significant results are plotted with fine (red) dots. (For interpretation of the references to color in this figure legend, the reader is referred to the web version of this article.)
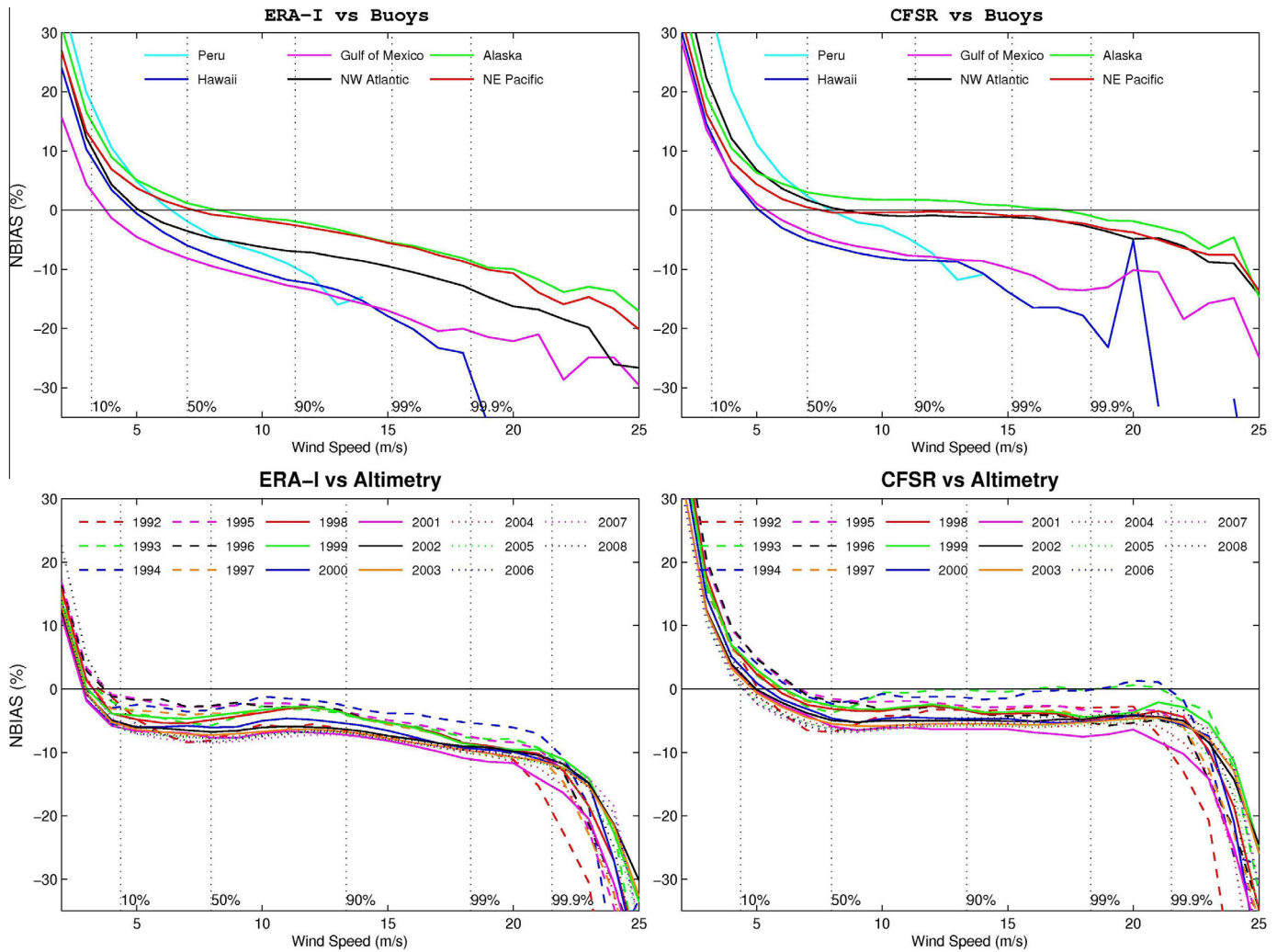
Fig. 9. Normalized biases as a function of wind speed. Dashed vertical lines are the average percentiles to indicate the amount of data the error metric represents.

Table 2
Error metrics for significant wave height at buoys using all available data during 1979–2009.

Significant wave height									
Region	n	Average (m)	Reanalysis	NBIAS (%)	RMSE (m)	CRMSE	COR	SI (%)	NSTD
Peru	68216	2.14	CFSR-W	24.77	0.62	0.29	0.88	13.70	1.14
			ERA-I	8.29	0.33	0.27	0.89	12.83	0.60
Hawaii	715116	2.37	CFSR-W	7.26	0.43	0.39	0.89	16.28	1.37
			ERA-I	−5.61	0.34	0.31	0.91	12.91	0.64
Gulf of Mexico	859929	1.11	CFSR-W	4.95	0.28	0.28	0.93	24.87	1.03
			ERA-I	−6.20	0.29	0.28	0.93	24.94	0.70
NW Atlantic	1035607	1.79	CFSR-W	2.36	0.39	0.39	0.93	21.54	0.86
			ERA-I	−6.87	0.42	0.39	0.94	22.02	0.65
Alaska	586911	2.83	CFSR-W	4.13	0.56	0.55	0.93	19.26	1.01
			ERA-I	−5.73	0.51	0.48	0.95	16.81	0.69
NE Pacific	718693	2.78	CFSR-W	10.79	0.57	0.46	0.95	16.55	1.15
			ERA-I	−1.23	0.43	0.43	0.96	15.32	0.70

Rascle and Ardhuin (2013) identified a discontinuity in 2007, this feature is not clearly discernible here despite the increasing bias from the GFO platform.

The time series comparisons indicate regional and seasonal variations of errors in the reanalysis datasets that we further investigate by computing normalized biases in 2° bins across the globe for the summer and winter seasons. Figs. 6 and 7 plot the computed biases against TPX measurements for December–January–February (DJF) and June–July–August (JJA) in the representative years of 1993, 1998, and 2003 during the platform operation. The results illustrate the overall spatial distribution of the errors and the seasonal extremes over a decade. In general, the biases of ERA-I and CFSR follow similar patterns with different levels of errors. Fig. 6 shows predominant positive biases in the

Southern Hemisphere during DJF. The positive bias is typically greater in CFSR than ERA-I with the largest difference of 10% in 1993. The negative bias near the Equator becomes the most dominant feature in 1998. This year coincides with the end of the strongest El Nino on record. Stopa et al. (2013) demonstrates distinct patterns of the climate cycle in CFSR, but the negative bias might represent small-scale processes that neither dataset is able to resolve. While the level and spatial expanse of the biases generally decrease over the years, CFSR still overestimates in the trade wind regions near Chile and East Africa and ERA-I underestimates the wind speed in the NW Pacific and NW Atlantic by 2003. Fig. 7 shows a reverse pattern in JJA with predominant positive biases of the two datasets in the Northern Hemisphere. The larger positive biases in CFSR extend to the Equatorial region in 10°S–10°N, while ERA-I has predominant negative biases in the Southern Hemisphere. In addition, ERA-I gives lower predictions of the wind speed than CFSR near 5–10°N in the Eastern Pacific and Atlantic. CFSR shows an overestimation of the Southern Hemisphere trade wind region offshore of Chile. The negative biases near the Equator associated with the El Nino of 1998 are not as prominent this time of year.

Some of the biases in Figs. 6 and 7 might stem from the interpolation and post-processing of the altimetry measurements. Artifacts from the ground tracks, which are spaced up to 240 km near the equator, result in non-physical features over larger patterns. In addition, the altimeter measures wind speed relative to sea surface currents, while the reanalysis winds reference a fixed position. This might introduce errors in areas with strong currents as identified by Chelton and Freilich (2005) in the QuikSCAT data. The ocean currents also influence the atmospheric boundary layer, which is assumed to be neutrally stable in deducing the recorded wind speed at the 10 m standard elevation. The consistent underestimation in

the Equatorial region 0–5°S may be attributed to instability of the boundary layer because of the warm sea surface and currents. Despite the limitations, both the negative and positive biases reduce showing improvement of the datasets over the years. Figs. 6 and 7 present the same features as the time series in Figs. 4 and 5 with overestimations in the summer and underestimations in the winter. These features are most notable in the Westerlies 30–60° of both hemispheres. Qualitatively the results suggest a decreasing trend of the errors for most regions. CFSR has the largest positive biases in the North Pacific and North Indian Ocean in 1993 and improves over time with a better match in 2003, while ERA-I biases remain relatively small across the globe with subtle improvements over the years. However, CFSR exhibits the largest range of errors in the Southern Ocean from positive biases in 1993 to negative in 2003. The biases in both datasets are generally within 15% (or 1.5 m/s) with the exception of the 1993 CFSR in the Southern Hemisphere.

The MK seasonal test with Sen's slope can quantify the negative trend of the wind speed biases against observations. The quality-controlled measurements from TPX and GFO extend from 1992 to 2008 to best match the period of ERA-I and CFSR. This allows assessment of the homogeneity of the datasets throughout the time series and across the globe. Instead of the bias, we consider the normalized monthly percentile to deduce the trends in terms of the severity of wind events. Fig. 8 plots the Sen's slope over 2° bins for the normalized 50th, 90th, and 99th percentiles of the two reanalysis datasets. A homogenous dataset should have a zero slope indicating no trend over time. The Sen's slope of all the percentiles for CFSR and ERA-I indicates a decreasing trend, which corroborate the general improvement of the reanalysis data through time. Both datasets have similar orders of magnitude and spatial
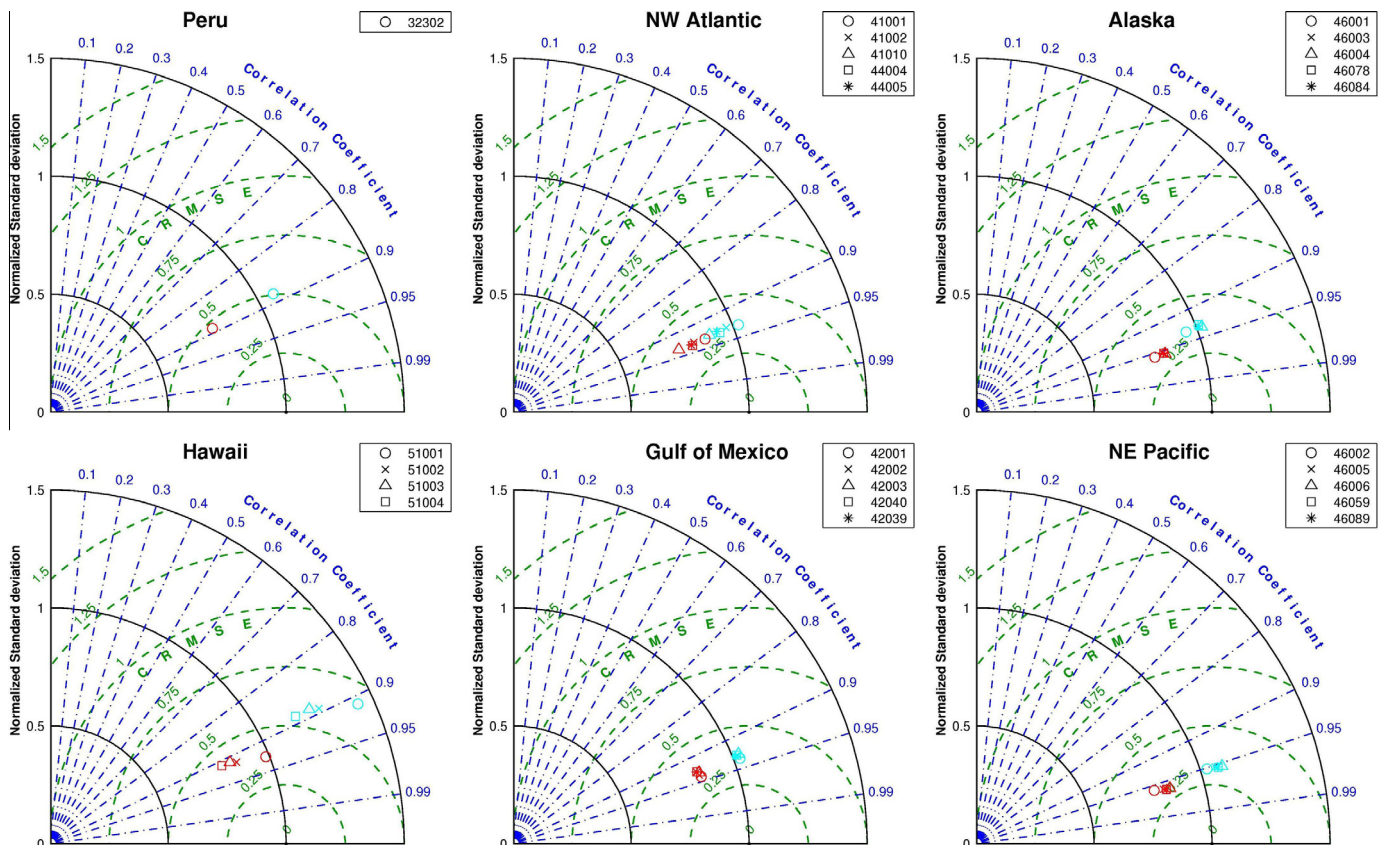

Fig. 10. Taylor diagram of error metrics for significant wave height at buoys grouped by region. Cyan symbols represent CFSR and red symbols represent ERA-I. A perfect model would lie on the *x*-axis with a NSTD equal to one.
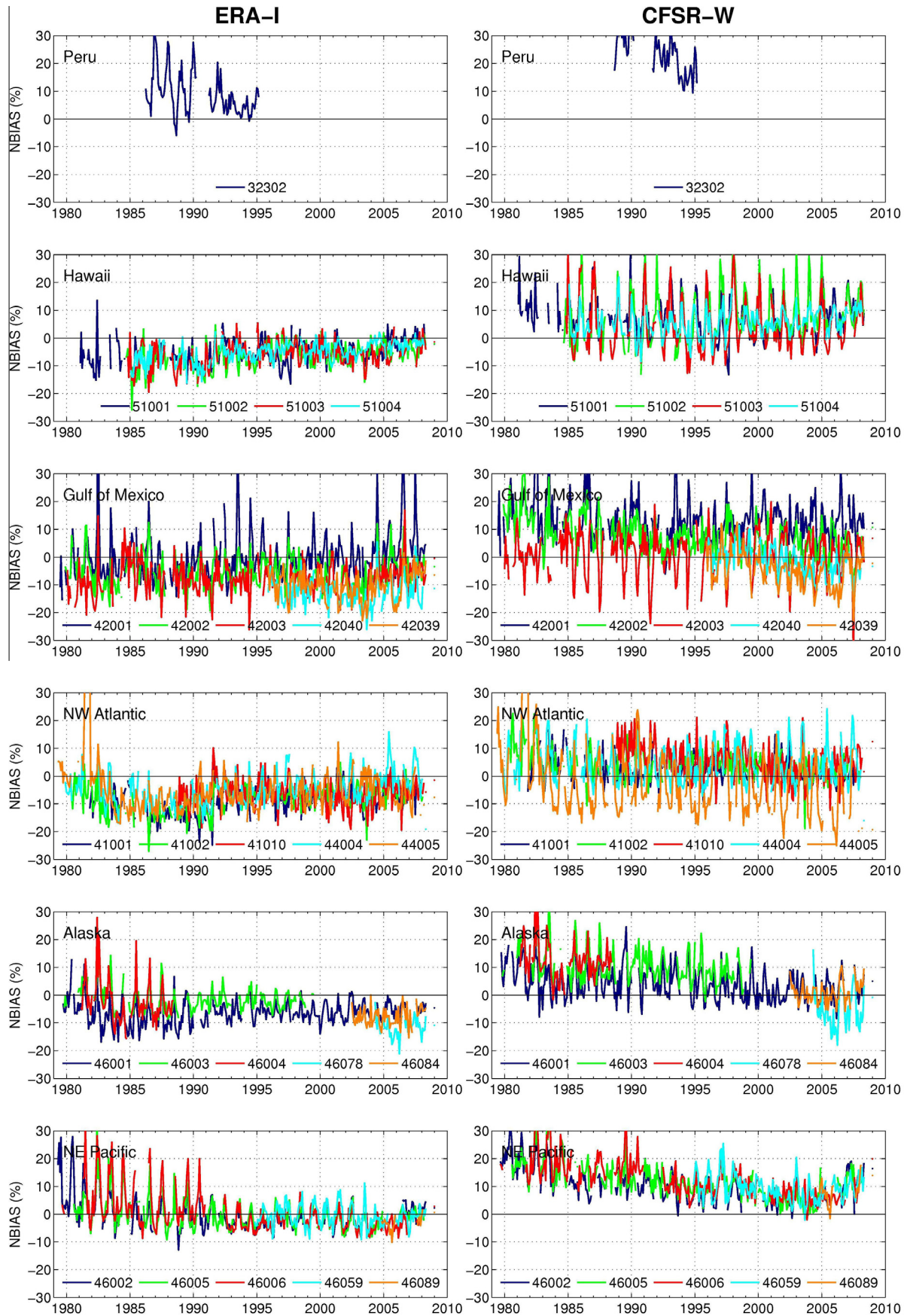
Fig. 11. Normalized wave height biases for buoys by region.

distribution for all percentiles from typical to strong winds. An exception occurs in the Equatorial region, which shows the largest decreasing trend with larger affected areas under CFSR. The MK seasonal test with α = 95% indicates there are few statistically significant values, which are plotted with a red "dot". The weak error trends confirm the homogeneity and consistency of the reanalysis datasets over time.

A quantitative approach to resolve the nonlinear behavior of the errors is to compute the biases in incremental bins of wind speeds. Fig. 9 plots the normalized biases of ERA-I and CFSR against buoy and altimetry measurements for binned wind speeds of 1 m/s. Available buoy data over time is grouped by region and all full years of altimetry data are used globally. The average percentiles of each observation group are calculated from all the data to give an estimate of the distribution for each region or year. Consistent with the results presented so far, both ERA-I and CFSR follow a similar pattern with overestimation of the lower wind speeds and underestimation of the upper wind speeds. However, sampling artifacts from computing the error metrics in incremental bins tend to exaggerate these features (Tolman, 1998). The sharp drop in the altimetry wind speed above 23 m/s may also be the result of the post-processing algorithm of the satellite data as already pointed out by Quilfen et al. (2006) and Hanafin et al. (2012). Despite the sampling artifacts and processing errors, the observations provide a common reference to evaluate the relative differences between the two datasets.

At the buoys, ERA-I gives lower predictions than CFSR with average biases of 3% to −10% between the 20th and 99th percentile across all regions. The upper 1% wind speeds diverge with larger negative errors and increasing variability among the regions. The CFSR gives larger positive biases in comparison to ERA-I at low percentiles; however these winds contribute little to the generation of waves. From the 20th to 99th percentile, CFSR matches the observations very well with 2% to −8% biases. The divergence occurs at higher percentiles in comparison to ERA-I. Data from altimetry exhibits similar features based on a larger bank of independent observations (4.0 million buoy records versus 6.9 million points for altimetry). The upper 10% of the ERA-I data shows increasing negative errors, while CFSR stays relatively consistent with small errors through the upper 99.8th percentile. The bulk of the data between 10 to 90th percentiles have average biases of −6% for ERA-I and -2% for CFSR. Since the upper percentile wind speeds are analyzed for engineering design or as indicators of climate change, caution must be exercised with ERA-I and CFSR above their respective 90th and 99.8th percentile thresholds.

4.2. Significant wave height

Now that the errors and trends of the ERA-I and CFSR wind datasets are quantified, we apply the same procedures to evaluate the wave datasets. The parallel assessment of the wave data in relation to the wind forcing provides general guidance of their
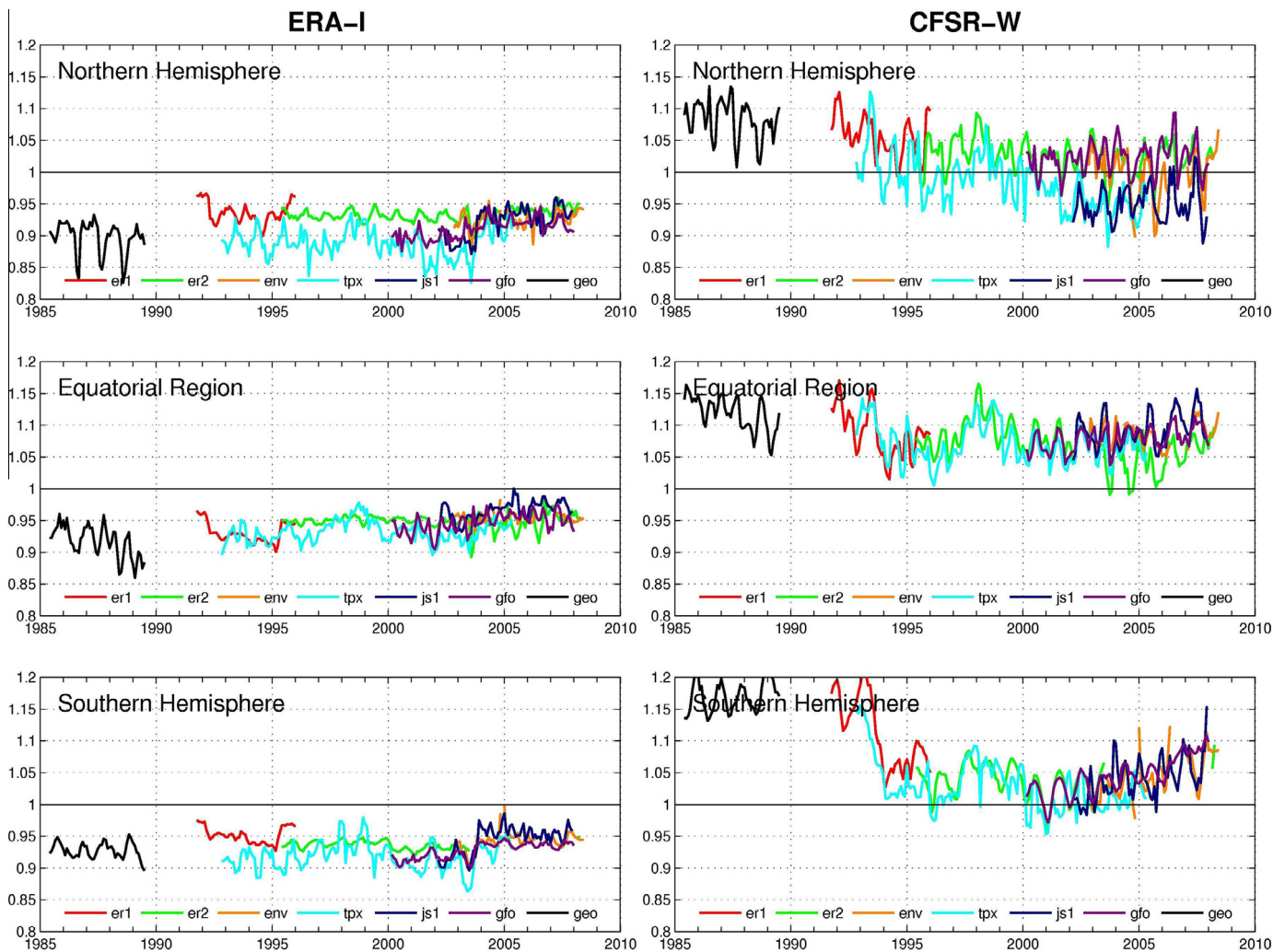

Fig. 12. The 95th percentile wave height normalized by altimetry observations and integrated across the Northern Hemisphere, Equatorial region, and Southern Hemisphere.

implementation for ocean modeling. Table 2 summarizes the error metrics of the significant wave heights from the two reanalysis datasets at the buoys. The error matrices are based on the same set of records as the wind intercomparison, but with slightly different numbers due to random data outage. The average recorded wave height ranges from 1.11 m in the Gulf of Mexico to 2.83 m near Alaska. The comparison is obscured by the respective wave models used in ERA-I and CFSR-W and to a lesser extent the assimilation of wave data in the former. Both datasets have small RMSEs on the order of 0.5 m, high correlation coefficients above 0.9, and comparable scattered indices in each region. ERA-I typically has lower wave heights indicated by the negative normalized biases, except near Peru, while CFSR-W shows systematic overestimations in all regions. As in the wind comparisons, large scatter indices of over 20% occur in regions such as Gulf of Mexico and NW Atlantic, which are susceptible to tropical cyclones. The high correlation coefficient over 0.93 suggests that the majority of storms are included in both datasets; however the intensity cannot be adequately resolved with the spatial grid resolution (Chawla et al. 2013). The Taylor diagrams in Fig. 10 show ERA-I have reduced errors and larger correlation coefficients, but typically underestimate the standard deviation of the buoy measurements by 30% due to the lower variability of the input winds. CFSR-W shows a better match to the variability of the observations with a predominant positive trend of the normalized standard deviation especially in

regions dominated by swell, such as Peru, Hawaii, NE Pacific. The consistent lower variability of ERA-I in comparison to observations is indicative of a smoother model that does not capture the extremes of weather processes.

Fig. 11 presents the monthly normalized biases of the significant wave height from the buoys to illustrate the variation of the errors over time. The seasonal cycle in the reanalysis winds is carried over to the waves. The wave data, which also includes distant swells, might not show direct correlation with the wind errors presented in the previous section. Offshore of Peru both CFSR-W and ERA-I have large positive biases over 30% in the beginning of the time series. Despite the short record, the errors appear to decrease and become less variable over time. Near Hawaii, ERA-I begins with persistent negative biases around −8% that improve with time to nearly zero. CFSR-W has predominant positive biases with large seasonal variations explaining the increased variability shown in the Taylor diagrams. The Gulf of Mexico is a semi-enclosed basin with limited fetch and locally generated waves. ERA-I and CFSR-W follow the pattern of the wind data in Fig. 4 with biases averaged approximately −7% and 6%. The variability in this region reflects the larger scatter index associated with the wind waves generated over short fetches as presented in Table 2. In the NW Atlantic, ERA-I have small negative biases while CFSR-W show positive biases throughout the time series. Both datasets have rather consistent errors with no obvious trend.
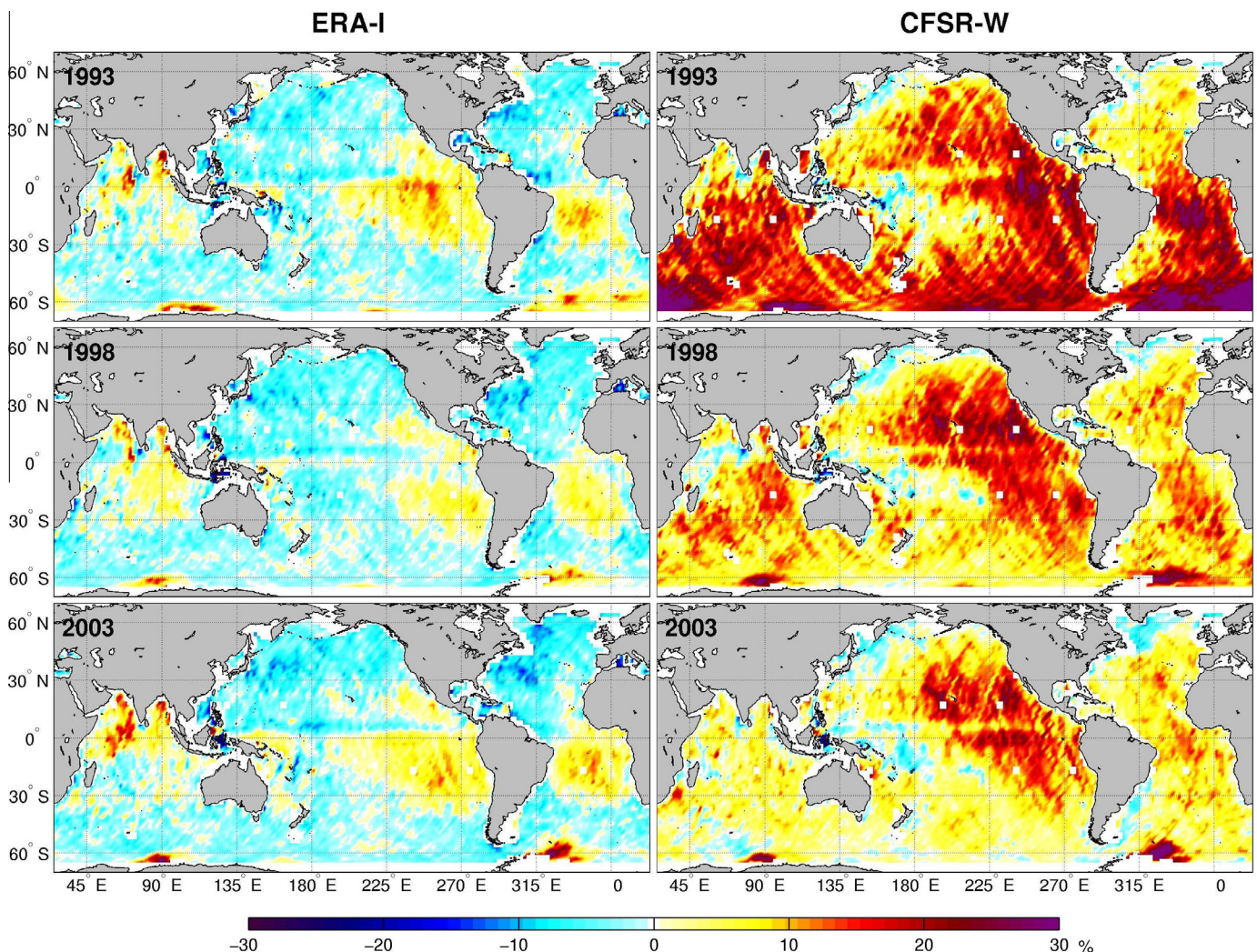

Fig. 13. Normalized wave height biases for TPX in December–January–February (DJF).

Extra-tropical storms dominate in the upper latitudes near Alaska. The biases in the wind and wave data show a similar pattern with values that are largest in the early 1980s and then decrease with time. ERA-I consistently underestimates the wave heights around 6%, while CFSR-W overestimates at 4%, but with a noticeable negative trend that results in more accurate prediction with time. The NE Pacific has similar patterns to Alaska with noticeable trends in both datasets and the predictions are more accurate in recent years. CFSR-W has positive biases at 10% throughout the time series while ERA-I has minimal negative biases. The region is dominated by swells. CFSR-W has more seasonal extremes with positive biases in the winter season as seen in other swell dominated environments like Hawaii. The increasing trend of the CFSR-W biases in these swell-dominated regions starting in 2007 is likely related to the shift of upper percentile winds in the reanalysis as noted by Chawla et al. (2013) and Rascle and Ardhuin (2013). The winds also account for some of the wave variability in the 1980s in both datasets most notably in Alaska and the NE Pacific. Weather patterns that might not be adequately resolved result in biases in both reanalysis datasets. For example, the biases at buoys 46001 in Alaska, and 46002, 46003, and 46006 in NE Pacific show cycles of 10 years that might be related to the Pacific Decadal Oscillation. Overall, both ERA-I and CFSR-W improve with time due to the better quantity and quality of data included in the assimilation.

Altimetry offers another view of the data error through time. Fig. 12 shows the monthly 95th percentile of the ERA-I and CFSR-W significant wave heights normalized by altimetry measurements from 1985 onward. It must be noted that GEO, TPX, and GFO were not used in the assimilation of ERA-I and thus are independent. In the Northern Hemisphere, ERA-I underestimates the waves by 8%, while CFSW shows an initial overestimation that decreases with time. Near the Equator, ERA-I underestimates the waves by approximately 6% with a better match in the 2000s. CFSR-W consistently overestimates the wave heights at approximately 7%. In the Southern Hemisphere, ERA-I has a similar underestimation to the Northern Hemisphere of 8% and an abrupt transition in 2004 to 5%. CFSR-W has a prominent discontinuity in 1993–1994 when the overestimation drops from 12% to 4% in the Southern hemisphere. This discontinuity is noticeable but not as drastic in other regions. Chawla et al. (2013) attributed the error reduction in the upper percentiles to the introduction of SSM/I winds into the assimilation in 1994 and the subsequent improvement in the wave field. The increasing trend in both datasets after 2001 might be due to assimilated data in the atmospheric model common to both.

The distribution of icebergs prominently in the Southern Ocean has strong inter-annual variability and might influence some of the trends in this region. Ice bergs also represent an error source with far-reaching effects extending to the Equator (Ardhuin et al. 2011). Extension of the obstructions technique to include icebergs can
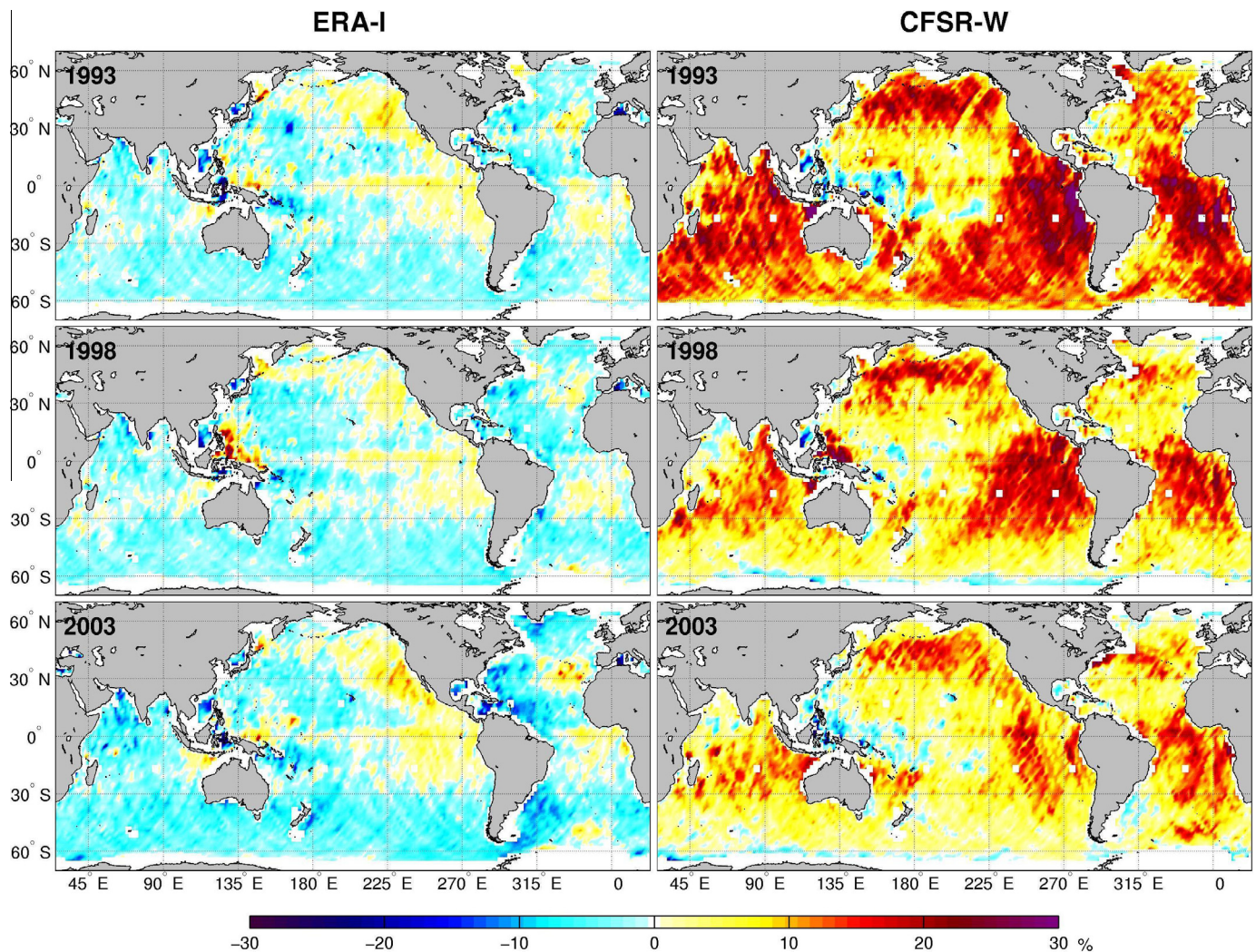

Fig. 14. Normalized wave height biases for TPX in June–July–August (JJA).

alleviate wave biases across ocean basins (Tolman 2003). The introduction of wave data assimilation in ERA-I in 1991 explains the slight improvement in metrics against the ER1, ER2, ENV, and JS1 observations, but does not seem to affect the results from the independent platforms. In general, ERA-I follows the pattern shown in the winds with a consistent underestimation. The CFSR winds match the altimetry winds reasonably well with even a minor underestimation, but the waves show a consistent overestimation for all regions. The lack of direct correlation between winds and waves alludes to difference caused by the source terms. More in-depth studies using the approach of Durrant et al. (2013) will help to isolate the effects of input wind biases and source terms on the wave field.

We compute the normalized biases against TPX measurements in 2° bins across the globe to examine the spatial variability associated with the summer and winter seasons. Figs. 13 and 14 plot the results for DJF and JJA in 1993, 1998, and 2003. The spatial distributions for ERA-I and CFSR-W are drastically different. Throughout the years in DJF, ERA-I has small negative biases around most of the globe with notable exceptions in the eastern tropical regions. The positive biases in these swell-dominated regions are likely due to the lack of swell dissipation in the WAM source terms (Bidlot et al., 2005). ERA-I has uniform errors of less than ±15% (0.5 m) through the years with only a slight increase of the negative biases in the Northern Hemisphere in 2003. In contrast, CFSR-W has large

positive biases for the majority of the globe with extremes of over 30% (~1 m) in 1993. The large positive biases occur in the wave generation regions dominated by the Westerlies in both hemispheres and propagate eastward in the ocean basins. The overestimation of the upper percentile CFSR winds in the Westerlies has far-reaching effects on the wave field across the basins. The areas sheltered from the swells in CFSR-W have errors more comparable to ERA-I's biases of ±15%. The CFSR-W errors decrease in magnitude and spatial coverage abruptly in the Southern Hemisphere in 1994 due to additional assimilation data for the winds from the SSM/I satellite.

The biases for JJA in Fig. 14 show a reverse pattern associated with the seasonality shown in the time series comparison. The majority of the globe shows negative biases in ERA-I with the main exception of the eastern Pacific and Atlantic basins between 30°S–30°N, where the wave fields are dominated by swells. The negative biases of 5–15% in the Southern Hemisphere are likely related to the wind speed underestimation of up to 10% as shown in Fig. 7. ERA-I has relatively stable errors with only a slight increase in the negative biases in the Southern Hemisphere through the years. On the other hand, CFSR-W has predominantly positive biases across the globe. The spatial distributions of the ERA-I and CFSR wind biases have similar patterns, but the wave biases are rather different alluding to the disproportionate effects of the upper percentile winds and the implementation of different source terms in
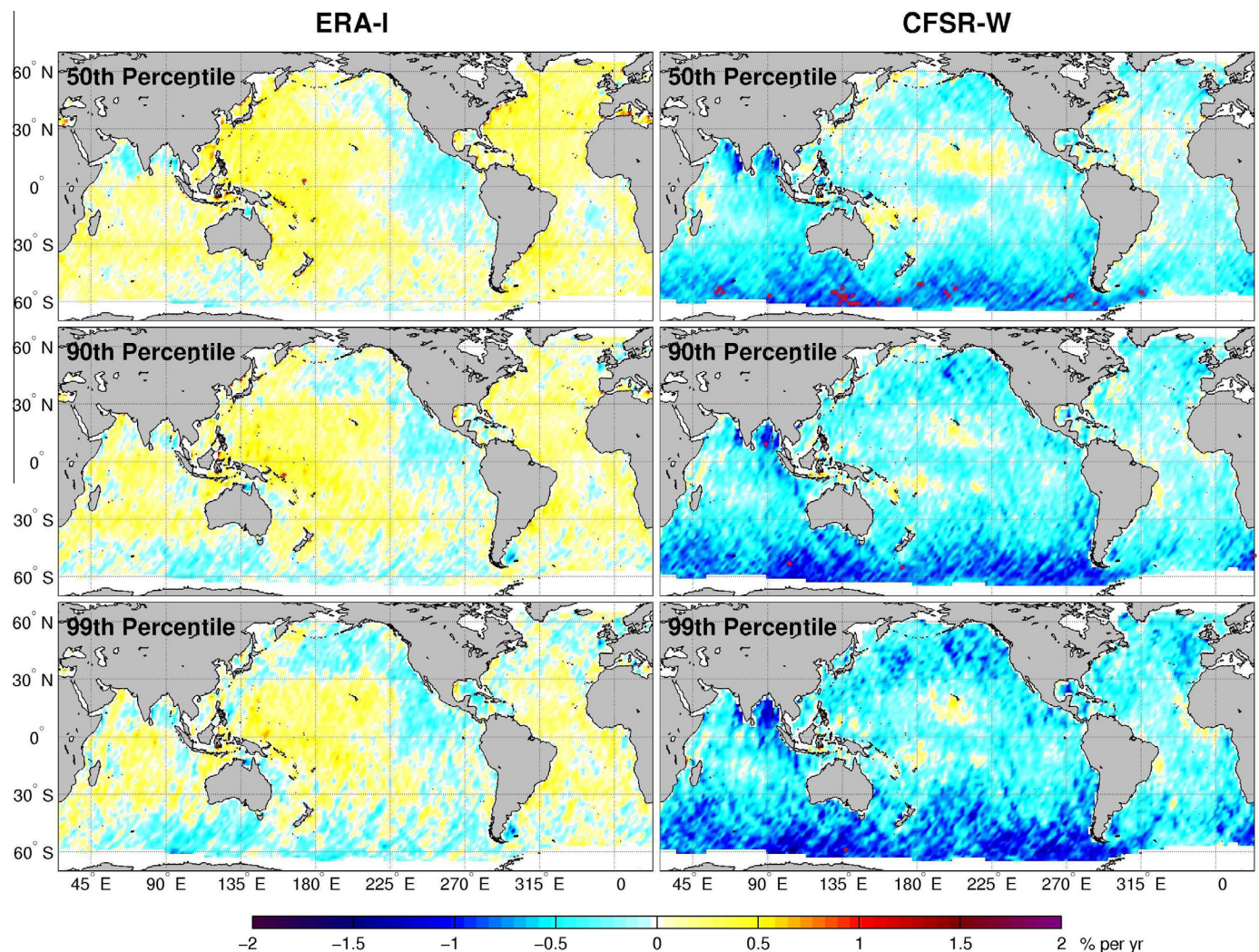

Fig. 15. Sen's slope with statistically significant results from the seasonal MK test of normalized monthly wave height percentiles using TPX and GFO. Statistically significant results are plotted with fine (red) dots. (For interpretation of the references to color in this figure legend, the reader is referred to the web version of this article.)

the wave models. In 1993, CFSR-W has large positive biases of over 20% covering the majority of the Southern Hemisphere and a region in the North Pacific. The biases intensify toward the eastern halves of the oceans and even extend into the Northern Hemisphere via propagation of swells. The same pattern exists through 2003 but the intensity of the errors is greatly reduced and CFSR-W is more accurate in recent years. In the absence of wind biases, Durrant et al. (2013) shows the source terms of Tolman and Chalikov (1996) actually provide slight underestimations across the majority of the oceans in contrast to the CFSR-W results in Figs. 13 and 14. This stresses the importance of having accurate wind forcing and implies the errors in the ERA-I and CFSR waves are primarily due to the wind input.

The analysis has demonstrated the seasonal and long-term trends in ERA-I and CFSR-W. The MK seasonal test with Sen's slope quantifies the trend against GEO, TPX, and GFO across the globe from 1985 to 2008. Fig. 15 plots the Sen's slope for the monthly 50th, 90th, and 99th percentiles of the significant wave height normalized by measurements and the statistically significant locations over 2° bins. The results reveal the spatial homogeneity of each product as well as the trends in terms of the severity of wave events through time. At a first glance, the Sen's slope and its spatial distribution are similar from the 50th to 99th percentiles for the respective products. This indicates the error trend has similar orders of magnitude in the bulk of each dataset. ERA-I has positive trends in the western half of the ocean basins and a negative trend

in east attributing to different wave regimes responsible for the errors. The Southern Ocean sees a negative trend that expands with higher percentiles, but the reason is obscured by the lack of accounting for icebergs in the model. There are no statistically significant points by the seasonal Mann–Kendall test revealing the product is reasonably homogenous through time. On the other hand, CFSR-W has predominantly negative trends across the globe particularly in the Southern Ocean with a few statistically significant bins near Australia in the 50th percentile. The strong discontinuity shown in Fig. 12 plays a tremendous role in the trend and this figure reveals the source of the errors primarily at latitudes greater than 30°S. The rest of the globe shows a small negative trend of less than 0.5% per year. The strong negative trend seen in the normalized wind percentiles near the Equator is not evident here because it is not a wave generation region.

Computation of the error metrics by incremental bins can reveal the error distribution in terms of the wave height. Fig. 16 plots the normalized biases against 4.0 and 4.5 million of buoy and altimetry measurements at binned significant wave height of 0.5 m. Normalized biases are computed for the buoys using the available periods by region and the individual years from GEO, TPX, and GFO across the globe. ERA-I and CFSR-W have similar patterns with overestimations for small wave heights and underestimations of large wave heights. In contrast to the wind comparison, the wave height shows a negative trend of the biases across all percentiles. The biases against the buoy measurements demonstrate the variability
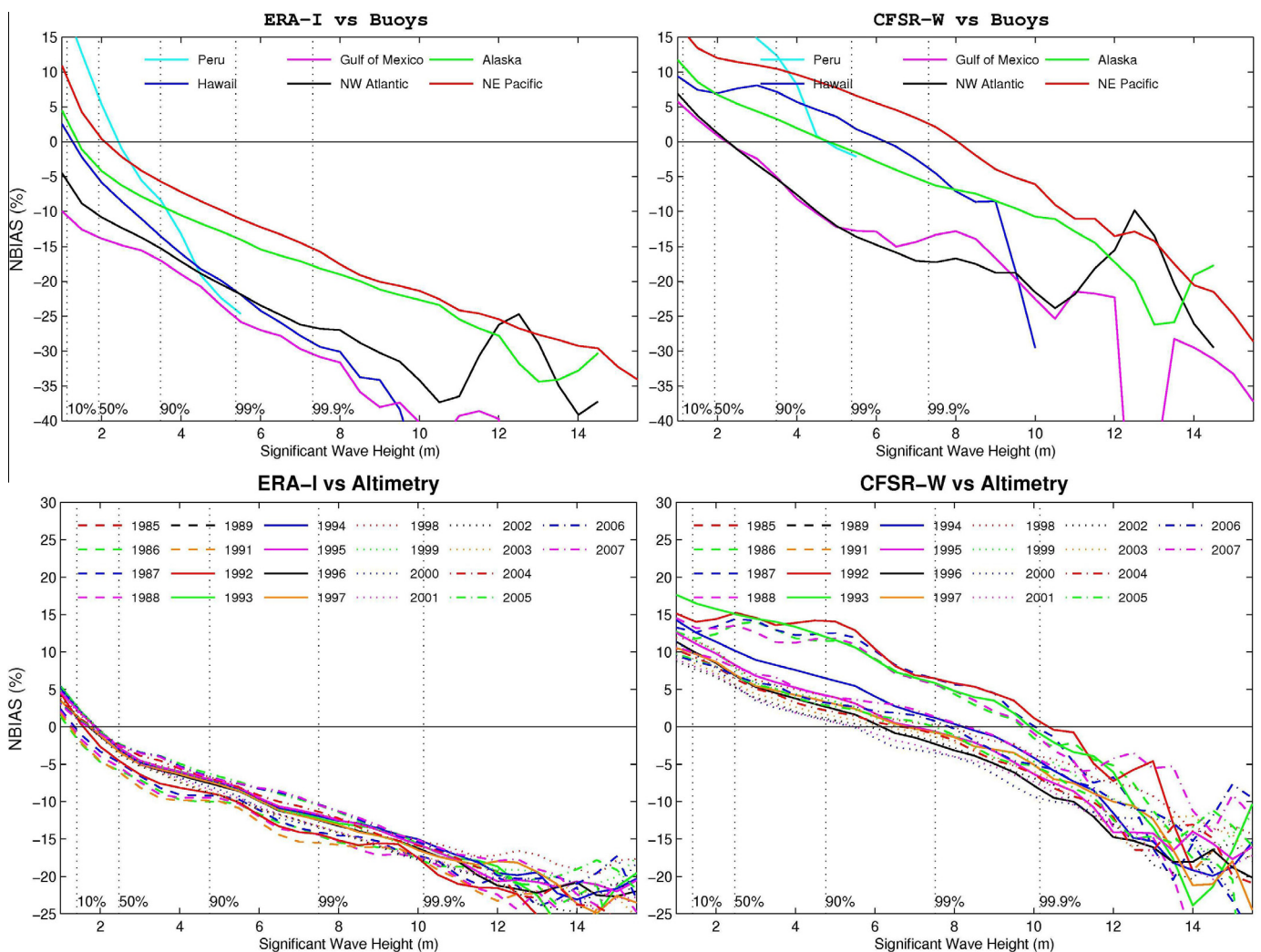

Fig. 16. Normalized biases as a function of wave height. Dashed vertical lines are the average percentiles to indicate the amount of data the error metric represents.

between regions, but overall, exhibit the same pattern around the globe and correspond well with the respective altimetry comparisons. The large variations above the 99.9th percentile are due to small numbers of data points. The biases against altimetry measurements integrated around the globe are consistent from year to year in the ERA-I data. However in the CFSR-W data, the years before 1994 typically have more positive biases due to the discontinuity discussed earlier. The second discontinuity in 2007 as identified by Rascle and Ardhuin (2013) only has subtle effects in the results. The biases between the 10th and 90th percentiles have a range of −8% to 5% for ERA-I versus 2 to 12% for CFSR-W after 1994. However, ERA-I underestimates the wave height by 5% to 18% for the upper percentiles between 90th and 99.9th that are crucial in evaluation of extremes. In comparison, CFSR-W has biases in a more favorable range of −8% to 4% for engineering applications and climate studies. If either dataset is used to estimate extreme events, like the 100-year design waves, barring occurrences of tropical cyclones that might not be resolved in either dataset, caution must be used in the analysis of these upper percentiles. The errors may be larger by using the ERA-I dataset because the errors at the upper 0.1% waves are nearly double to those of CFSR-W.

5. Conclusions and recommendations

The ERA-I and CFSR-W reanalysis datasets have improved performance over their predecessors and have many applications due to the high spatial resolutions and long durations of over 30 years. Their intercomparison with buoy and altimetry measurements has identified systematic seasonal biases, temporal discontinuities, and spatial error trends in terms of wind speed and wave height. Time series plots of error metrics expose the temporal homogeneity around the globe. The dominant features include large seasonal cycles with negative biases in high seasons and vice versa, strong variability in the 1980s, and an overall trend that leads to improvement over time. Both datasets compare reasonably well at the buoys and altimetry tracks with ERA-I underestimating and CFSR-W overestimating the measurements. CFSR-W shows an abrupt drop of the high-percentile wind speed to provide better agreement in the Southern Ocean in 1994 due to additional assimilation data. The improvement to the regional wind predictions has far-reaching effects on the wave field across the ocean basin. CFSR-W has considerable more seasonal variations in the waves and better agreement with buoy measurements than ERA-I despite having similar features in the winds. The consistently lower variability of ERA-I implies a smoother data set lacking detailed processes and weather extremes. The buoy comparisons in the Gulf of Mexico have the largest variability suggesting poor model performance for small fetches.

The biases of ERA-I and CFSR-W against altimetry measurements demonstrate the spatial distribution and seasonal variation of the contributing errors over the years. Both datasets show largest discrepancies of the relatively calm and variable winds near the Equator that might be a result of the observations not explicitly accounting for atmosphere stability. CFSR-W gives consistently higher predictions of the winds in the Westerlies that carry over to the wave predictions extending to the swell-dominated regions. The error metrics reveal that ERA-I has similar errors through time, while CFSR-W has a negative trend with the predictions getting more accurate in recent years. The seasonal MK test with the Sen's slope quantifies the error trend and demonstrates its independence of the severity of the wind and wave events implying performance consistency of both datasets. Both wind datasets show the largest negative trends in the Equatorial region that are not important to the dominant wave conditions. The ERA-I wave data indicate

a small Sen's slope with minimal statistically significant points from the MK test indicating homogeneity through time, but localized spatial inhomogeneities might exist due to the assimilated wave data. CFSR-W has larger Sen's slope most notably in the Southern Ocean due to the discontinuity in 1994.

The errors for incremental wind speeds and wave heights confirm both datasets overestimate the small measurements and underestimate the large. CFSR-W has consistently higher predictions and matches the upper 50th percentiles better than ERA-I deeming its reliability in analysis of extremes. Both ERA-I and CFSR wind datasets have better agreement with the measurements than the wave datasets between the 10th and 99th percentiles and a diverging feature in the upper percentile waves heights. In summary, ERA-I is suitable for studies of multi-year signals and climate cycles and CFSR-W has additional capabilities for analysis of the extremes but caution must be taken with the discontinuity. Future wave hindcasting efforts with CFSR will have to correct the temporal discontinuity of the winds and utilize updated source terms to properly account for the dissipation of swell energy. This should also mitigate the seasonal biases in the computed wave conditions. Additional and improved measurements of the winds and waves will provide further insights and explanations in areas with large model errors. The methodology and results presented in this paper provide a template and a benchmark for evaluation of improved or future reanalysis datasets.

Appendix A. Supplementary data

Supplementary data associated with this article can be found, in the online version, at http://dx.doi.org/10.1016/j.ocemod.2013.12. 006.

References

Ardhuin, F., Herbers, T.H.C., Watts, K.P., van Vledder, G.P., Jensen, R., Graber, H., 2007. Swell and slanting fetch effects on wind wave growth. J. Phys. Oceanogr. 37 (4), 908–931.

Ardhuin, F., Tournadre, J., Queffeulou, P., Girard-Ardhuin, F., Collard, F., 2011. Observation and parameterization of small icebergs: drifting breakswaters in the Southern Ocean. Ocean Modell. 39 (3–4), 405–410.

Bidlot, J.-R., Janssen, P.A.E.M., Abdalla, S., 2005. A revised formulation for ocean wave dissipation in CY29R1. ECMWF Technical, Memorandum R60.9/JB/0 (1): 1–35.

Bidlot, J.-R., Janssen, P.A.E.M., Abdalla, S., 2007. A revised formulation of ocean wave dissipation and its model impact. ECMWF Technical, Memorandum 509.

Bromirski, P.D., Cayan, D.R., Flick, R.E., 2005. Wave spectral energy variability in the northeast Pacific. J. Geophys. Res. 110 (C0), 3005. http://dx.doi.org/10.1029/2004JC002398.

Caires, S., Sterl, A., Bidlot, J.-R., Graham, N., Swail, V., 2004. Intercomparison of different wind–wave reanalysis. J. Clim. 17 (10), 1893–1913.

Chawla, A., Tolman, H.L., 2008. Obstruction grids for spectral wave models. Ocean Modell. 22 (1), 12–25.

Chawla, A., Spindler, D.M., Tolman, H.L., 2013. Validation of a thirty year reanalysis using climate forecast system reanalysis winds. Ocean Modell. 70, 189–206.

Chelton, D.B., Freilich, M.H., 2005. Scatterometer-based assessment of 10-m wind analyses from the operational ECMWF and NCEP numerical weather prediction models. Mon. Weather Rev. 133, 409–429.

Chen, G., Chapron, B., Ezraty, R., Vandemark, D., 2002. A global view of swell and wind sea climate in the ocean by satellite altimeter and scatterometer. J. Atmos. Ocean. Technol. 19 (11), 1849–1859.

Cox, A.T., Swail, V.R., 2001. A global wave hindcast over the period 1958–1997: validation and climate assessment. J. Geophys. Res. – Oceans 106 (C2), 2313–2329. http://dx.doi.org/10.1175/JCLI3775.1.

Dee, D.P., Uppala, S.M., Simmons, A.J., et al., 2011. The ERA-interim reanalysis: configuration and performance of the data assimilation system. Q. J. R. Meteorol. Soc. 137 (656), 553–597.

Durrant, T.H., Greenslade, D.J.M., Simmonds, I., 2013. The effect of statistical wind corrections on global wave forecasts. Ocean Modell. 70, 116–131.

Ek, M.B., Mitchell, K.E., Lin, Y., Rogers, E., Grunmann, P., Koren, V., Gayno, G., Tarplay, J.D., 2003. Implementation of Noah land surface model advances in the National Centers for Environmental Prediction operational mesoscale Eta model. J. Geophys. Res. 108 (D22). http://dx.doi.org/10.1029/2002JD003296.

Genmrich, J., Thomas, B., Bouchard, R., 2011. Observational changes and trends in the northeast Pacific wave records. Geophys. Res. Lett. 38, L22601. http://dx.doi.org/10.1029/2011GL049518.

Gilbert, R.O., 1987. Statistical Methods for Environmental Pollution Monitoring. John Wiley and Sons, New York.

Gourrion, J., Vandemark, D., Bailey, S., Chapron, B., Gommenginger, G.P., Challenor, P.G., Srokosz, M.A., 2002. A two-parameter wind speed algorithm for Ku-band altimeters. J. Atmos. Ocean. Technol. 19 (12), 2030–2048.

Gulev, S.K., Grigorieva, V., Sterl, A., Woolf, D., 2003. Assessment of the reliability of wave observations from voluntary observing ships: insights from the validation of a global wind wave climatology based on voluntary observing ship data. J. Geophys. Res. 108 (C1), 3236. http://dx.doi.org/10.1029/2002JC001437.

Hanafin, J.A., Quilfen, Y., Ardhuin, F., Sienkiewicz, J., Queffeulous, P., Obrebski, M., Chapron, B., Reul, N., Collard, F., Corman, D., de Azevedo, E., Vandemark, D., Stutzmann, E., 2012. Phenomenal sea states and swell from a North Atlantic storm in February 2011: a comprehensive analysis. Bull. Am. Meteorol. Soc. 93 (12), 1825–1832.

Hasselmann, K., Hasselmann, S., 1991. On the nonlinear mapping of an ocean wave spectrum into a synthetic aperture radar image spectrum. J. Geophys. Res. 96 (C6), 10713–10729. http://dx.doi.org/10.1029/91JC00302.

Hemer, M.A., Church, J.A., Hunter, J.R., 2010. Variability and trends in the directional wave climate of the Southern Hemisphere. Int. J. Climatol. 30 (4), 475–491.

Hines, K.M., Bromwich, D.H., Marshall, G.J., 2000. Artificial surface pressure trends in the NCEP-NCAR reanalysis over the Southern Ocean and Antarctica. J. Clim. 13 (22), 3940–3952.

Hirsch, R.M., Slack, J.R., Smith, R.A., 1982. Techniques of trend analysis for monthly water-quality data. Water Resour. Res. 18 (1), 107–121.

Hwang, P.A., Toporkov, J.V., Sletten, M.A., Menk, S.P., 2013. Mapping surface currents and waves with interferometric synthetic aperture radar in coastal waters: observations of wave breaking in swell-dominant conditions. J. Phys. Oceanogr. 43 (3), 563–582.

Janssen, P.A.E.M., 1991. Quasi-linear theory of wind-wave generation applied to wave forecasting. J. Phys. Oceanogr. 21 (11), 1631–1642.

Janssen, P.A.E.M., 2008. Progress in ocean wave forecasting. J. Comput. Phys. 22 (7), 3572–3594.

Kalnay, E., Kanamitsu, M., Kistler, R., et al., 1996. The NCEP/NCAR 40-year reanalysis project. Bull. Am. Meteorol. Soc. 77 (3), 437–471.

Kanamitsu, M., Ebisuzaki, W., Woollen, J., Yang, S.K., Hnilo, J.J., Fiorino, M., Potter, G.L., 2002. NCEP–DOE AMIP-II reanalysis (R-2). Bull. Am. Meteorol. Soc. 83 (11), 1631–1643.

Kendal, M.G., 1975. Rank Correlation Methods, fourth ed. Charles Griffin, London.

Kistler, R., Kalnay, E., Collins, W., et al., 2001. The NCEP-NCAR 50-year reanalysis: monthly means CD-ROM and documentation. Bull. Am. Meteorol. Soc. 82 (2), 247–267.

Kleist, D.T., Parrish, D.F., Derber, J.C., Treadon, R., Errico, R.M., Yang, R., 2009. Improving incremental balance in the GSI 3DVAR analysis system. Mon. Weather Rev. 137 (3), 1046–1060.

Mann, H.B., 1945. Non-parametric tests against trend. Econometrica 13, 245–259.

Menendez, M., Mendez, F.J., Losada, I.J., Graham, N.E., 2008. Variability of extreme wave heights in the northeast Pacific Ocean based on buoy measurements. Geophys. Res. Lett. 35, L22607. http://dx.doi.org/10.1029/2008GL035394.

Queffeulou, P., Croizé-fillon, D., 2012. Global altimeter SWH data set – Version 9.0, IFREMER Tech Report: 1-8.

Quilfen, Y., Tournadre, J., Chapron, B., 2006. Altimeter dual-frequency observations of surface winds, waves, and rain rate in tropical cyclone Isabel. J. Geophys. Res. 111 (C1) (Article C01004).

Rascle, N., Ardhuin, F., 2013. A global wave parameter database for geophysical applications. Part 2: Model validation with improved source term parameterization. Ocean Modell. 70, 174–188.

Reguero, B.G., Menendez, M., Mendez, F.J., Minguez, R., Losada, I.J., 2012. A global ocean wave (GOW) calibrated reanalysis from 1948 onwards. Coastal Eng. 65, 38–55.

Saha, S., Moorthi, S., Pan, H.L., et al., 2010. The NCEP climate forecast system reanalysis. Bull. Am. Meteorol. Soc. 91 (8), 1015–1057.

Sen, P.K., 1968. Estimates of the regression coefficient based on Kendall's tau. J. Am. Stat. Assoc. 63, 1379–1389.

Sterl, A., Komen, G.J., Cotton, D., 1998. 15 years of global wave hindcasts using ERA winds: validating the reanalyzed winds and assessing the wave climate. J. Geophys. Res. 103 (C3), 5477–5492.

Sterl, A., 2004. On the (in)homogeneity of reanalysis products. J. Clim. 17 (19), 3866–3873.

Stopa, J.E., Cheung, K.F., Tolman, H.L., Chawla, A., 2013. Patterns and cycles in the climate forecast system reanalysis wind and wave data. Ocean Modell. 70, 207–220.

Taylor, K.E., 2001. Summarizing multiple aspects of model performance in a single diagram. J. Geophys. Res. 106 (D7), 7183–7192.

Tolman, H.L., Chalikov, D.V., 1996. Source terms in a third-generation wind–wave model. J. Phys. Oceanogr. 26 (11), 2497–2518.

Tolman, H.L., 1998. Effects of observation errors in linear regression and bin-average analyses. Q. J. R. Meteorol. Soc. 124 (547), 897–917.

Tolman, H.L., Balasubramaniyan, B., Burroughs, L.D., Chalikov, D.V., Chao, Y.Y., Chen, H.S., Gerald, V.M., 2002. Development and implementation of wind generated ocean surface wave models at NCEP. Weather Forecast. 17 (2), 311–333.

Tolman, H.L., 2003. Treatment of unresolved islands and ice in wind wave models. Ocean Modell. 5 (3), 219–231.

Tolman, H.L., Banner, M.L., Kaihatu, J.M., 2013. The NOPP operational wave model improvement project. Ocean Modell. 70, 2–10.

Uppala, S.M., Kallberg, P.W., Simmons, A.J., et al., 2005. The ERA-40 re-analysis. Q. J. R. Meteorol. Soc. 131 (612), 2961–3012.

WAMDIG, 1988. The WAM model – a third generation ocean wave prediction model. J. Phys. Oceanogr. 18 (12), 1775–1810.

Wang, X.L., Swail, V.R., 2001. Changes of extreme wave heights in Northern Hemisphere Oceans and related atmospheric circulation regimes. J. Clim. 14 (10), 2204–2221.

Whitaker, J.S., Compo, G.P., Thepaut, J.-N., 2009. A comparison of variational and ensemble-based data assimilation systems for reanalysis of sparse observations. Mon. Weather Rev. 137 (6), 1991–1999.

Woodruff, S.D., Diaz, H.F., Elms, J.D., Worley, S.J., 1998. COADS release 2 data and metadata enhancements for improvements of marine surface flux fields. Phys. Chem. Earth 23 (5–6), 517–526.

Woolf, D.K., Challenor, P.G., Cotton, P.D., 2002. Variability and predictability of the North Atlantic wave climate. J. Geophys. Res. 107 (C10), 3145. http://dx.doi.org/10.1029/2001JC001124.

Wu, X., Moorthi, K.S., Okomoto, K., Pan H.L., 2005. Sea ice impacts on GFS forecasts at high latitudes. In: Eighth Conference on Polar Meteorology and Oceanography, San Diego, CA, American Meteorological Society, 7.4 (Preprints).

Viterbo, P., Betts, A.K., 1999. Impact on ECMWF forecasts of changes to the albedo of the boreal forests in the presence of snow. J. Geophys. Res. – Atmos. 104 (D22), 27803–27810. http://dx.doi.org/10.1029/1998JD200076.

Yang, F., Pan, H.L., Krueger, S.K., Moorthi, S., Lord, S.J., 2006. Evaluation of the NCEP global forecast system at the ARM SGP site. Mon. Weather Rev. 134 (12), 3668–3690.

Young, I.R., 1999. Seasonal variability of the global ocean wind and wave climate. Int. J. Climatol. 19 (9), 931–950.

Young, I.R., Zieger, S., Babanin, A.V., 2011. Global trends in wind speed and wave height. Science 332 (6028), 451–455.

Zieger, S., Vinoth, J., Young, I.R., 2009. Joint calibration of multiplatform altimeter measurements of wind speed and wave height over the past 20 years. J. Atmos. Ocean. Technol. 26 (12), 2549–2564.